Distinct subsets of multi-lymphoid progenitors support ontogeny-related changes in human lymphopoiesis

Seydou Keita, Samuel Diop, Shalva Lekiashvili, Emna Chabaane, Elisabeth Nelson, Marion Strullu, Chloé Arfeuille, Fabien Guimiot, Thomas Domet, Sophie Duchez, et al.

Cell Reports

Article

Distinct subsets of multi-lymphoid progenitors support ontogeny-related changes in human lymphopoiesis

Graphical abstract

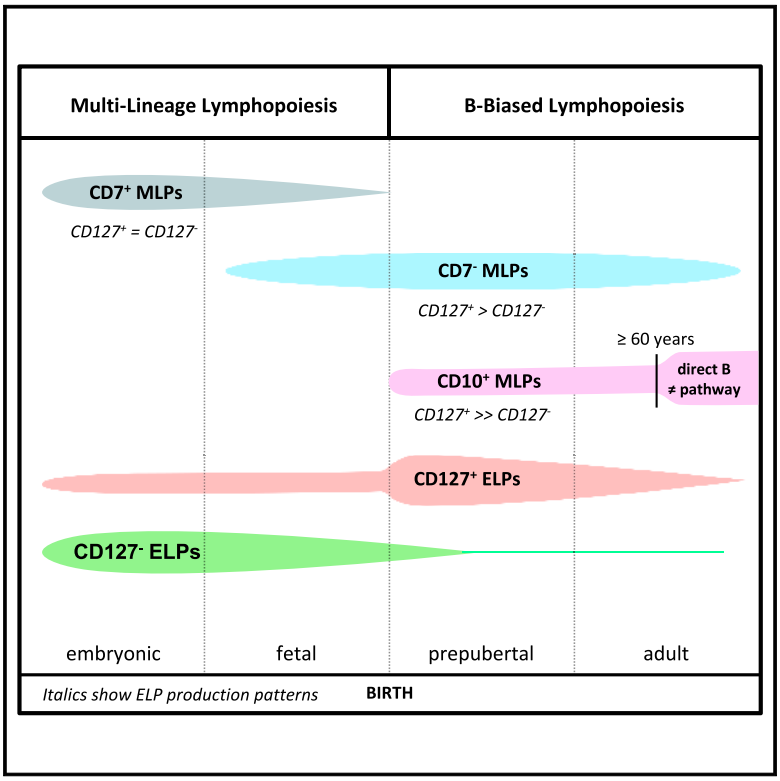

Highlights

- Distinct CD7$^{-/+}$CD10$^{-/+}$ MLPs support embryonic, fetal, and postnatal lymphopoiesis
- Embryonic, fetal, and postnatal MLPs differ in their ELP production patterns
- Transition to postnatal life coincides with a B-lineage shift of lymphopoiesis
- Ontogeny-related changes in lymphopoiesis are imprinted at the level of HSCs

Authors

Seydou Keita, Samuel Diop, Shalva Lekiashvili, ..., Frederic Chalmel, Kutaiba Alhaj Hussen, Bruno Canque

Correspondence

kutaiba.alhajhussen@aphp.fr (K.A.H.), bruno.canque@ephe.psl.eu (B.C.)

In brief

Keita et al. analyze the changes in lymphoid architecture and lymphocyte production patterns in 140 donors between 13 development weeks and 87 years. In addition to identifying embryonic, fetal, and postnatal MLP subsets, they show that the transition to postnatal life is associated with a B-lineage shift of lymphopoiesis.

Keita et al., 2023, Cell Reports *42*, 112618
June 27, 2023
https://doi.org/10.1016/j.celrep.2023.112618

CellPress

Cell Reports

CellPress
OPEN ACCESS

Article

Distinct subsets of multi-lymphoid progenitors support ontogeny-related changes in human lymphopoiesis

Seydou Keita,[1] Samuel Diop,[1,2] Shalva Lekiashvili,[1] Emna Chabaane,[1] Elisabeth Nelson,[1] Marion Strullu,[3] Chloé Arfeuille,[3] Fabien Guimiot,[4] Thomas Domet,[5] Sophie Duchez,[6] Bertrand Evrard,[7] Thomas Darde,[8] Jerome Larghero,[5] Els Verhoeyen,[9,10] Ana Cumano,[11] Elizabeth A. Macintyre,[12] Zeinab Kasraian,[12] François Jouen,[2] Michele Goodhardt,[1] David Garrick,[1] Frederic Chalmel,[7] Kutaiba Alhaj Hussen,[1,13,14,*] and Bruno Canque[1,14,15,*]

[1]INSERM U976, Université de Paris, École Pratique des Hautes Études/PSL Research University, Institut de Recherche Saint Louis, Paris, France

[2]Laboratoire Cognitions Humaine et Artificielle (CHArt) EA 4004 FED 4246, École Pratique des Hautes Études/PSL Research University, Paris, France

[3]Service d'Hémato-Immunologie Pédiatrique, Inserm U1131, Université de Paris, Hôpital Robert-Debré, AP-HP, Paris, France

[4]INSERM UMR 1141, Service de Biologie du Développement, Université de Paris, Hôpital Robert-Debré, AP-HP, Paris, France

[5]AP-HP, Hôpital Saint-Louis, Unité de Thérapie Cellulaire, CIC de Biothérapies, Université de Paris, INSERM U976, Paris, France

[6]Plateforme d'Imagerie et de Tri Cellulaire, Institut de Recherche Saint Louis, Paris, France

[7]INSERM, EHESP, IRSET (Institut de Recherche en Santé, Environnement et Travail), UMR_S 1085, University Rennes, Rennes, France

[8]SciLicium, Rennes, France

[9]CIRI, International Center for Infectiology Research, Université de Lyon, INSERM U1111, Lyon, France

[10]Centre Mediterranéen de Médecine Moléculaire (C3M), INSERM U1065, Nice, France

[11]Unit of Lymphopoiesis, Immunology Department, Institut Pasteur, Paris, France

[12]Institut Necker Enfants-Malades, Team 2, INSERM Unité 1151, Hôpital Necker Enfants-Malades, Laboratoire d'Onco-Hématologie, Assistance Publique-Hôpitaux de Paris (AP-HP), Université de Paris, Paris, France

[13]Service de Biochimie, Université de Paris Saclay, Hôpital Paul Brousse, AP-HP, Paris, France

[14]These authors contributed equally

[15]Lead contact

*Correspondence: kutaiba.alhajhussen@aphp.fr (K.A.H.), bruno.canque@ephe.psl.eu (B.C.)

https://doi.org/10.1016/j.celrep.2023.112618

SUMMARY

Changes in lymphocyte production patterns occurring across human ontogeny remain poorly defined. In this study, we demonstrate that human lymphopoiesis is supported by three waves of embryonic, fetal, and postnatal multi-lymphoid progenitors (MLPs) differing in CD7 and CD10 expression and their output of $CD127^{-/+}$ early lymphoid progenitors (ELPs). In addition, our results reveal that, like the fetal-to-adult switch in erythropoiesis, transition to postnatal life coincides with a shift from multilineage to B lineage-biased lymphopoiesis and an increase in production of $CD127^{+}$ ELPs, which persists until puberty. A further developmental transition is observed in elderly individuals whereby B cell differentiation bypasses the $CD127^{+}$ compartment and branches directly from $CD10^{+}$ MLPs. Functional analyses indicate that these changes are determined at the level of hematopoietic stem cells. These findings provide insights for understanding identity and function of human MLPs and the establishment and maintenance of adaptative immunity.

INTRODUCTION

The concept of developmental stratification of the immune system was first proposed by Herzenberg and Herzenberg on the basis of studies demonstrating the fetal origin of murine B1 lymphocytes.[1,2] Work over the past decade has shown that like B1 lymphocytes,[3] group 3 innate lymphoid cells (ILC3), and $V\gamma5^{+}/\gamma6^{+}$ T cells develop exclusively during embryonic life.[4] In mice, lymphoid specification is initiated downstream of hematopoietic stem cells (HSCs) in lymphoid-primed multipotent progenitors (LMPPs)[5,6] which lose myeloid potential as they upregulate the interleukin-7 (IL-7) receptor α-chain and differentiate into lymphoid-primed progenitors (LPPs) and then common lymphoid progenitors (CLPs).[7] These subsequently segregate into common helper innate lymphoid cell progenitors (CHILPs), thymus settling progenitors (TSPs), and early B cell progenitors (EBPs).[8] Despite evidence that mouse T and B cell precursors emerge asynchronously in fetal liver[9] and that thymus colonization is ensured by successive waves of T/ILC-restricted and multipotent TSPs,[8] it is currently unclear whether these changes are exclusively related to different stem/progenitor cell origins or if they could also reflect age-related variations in the lymphoid potential of definitive HSCs.[10,11]

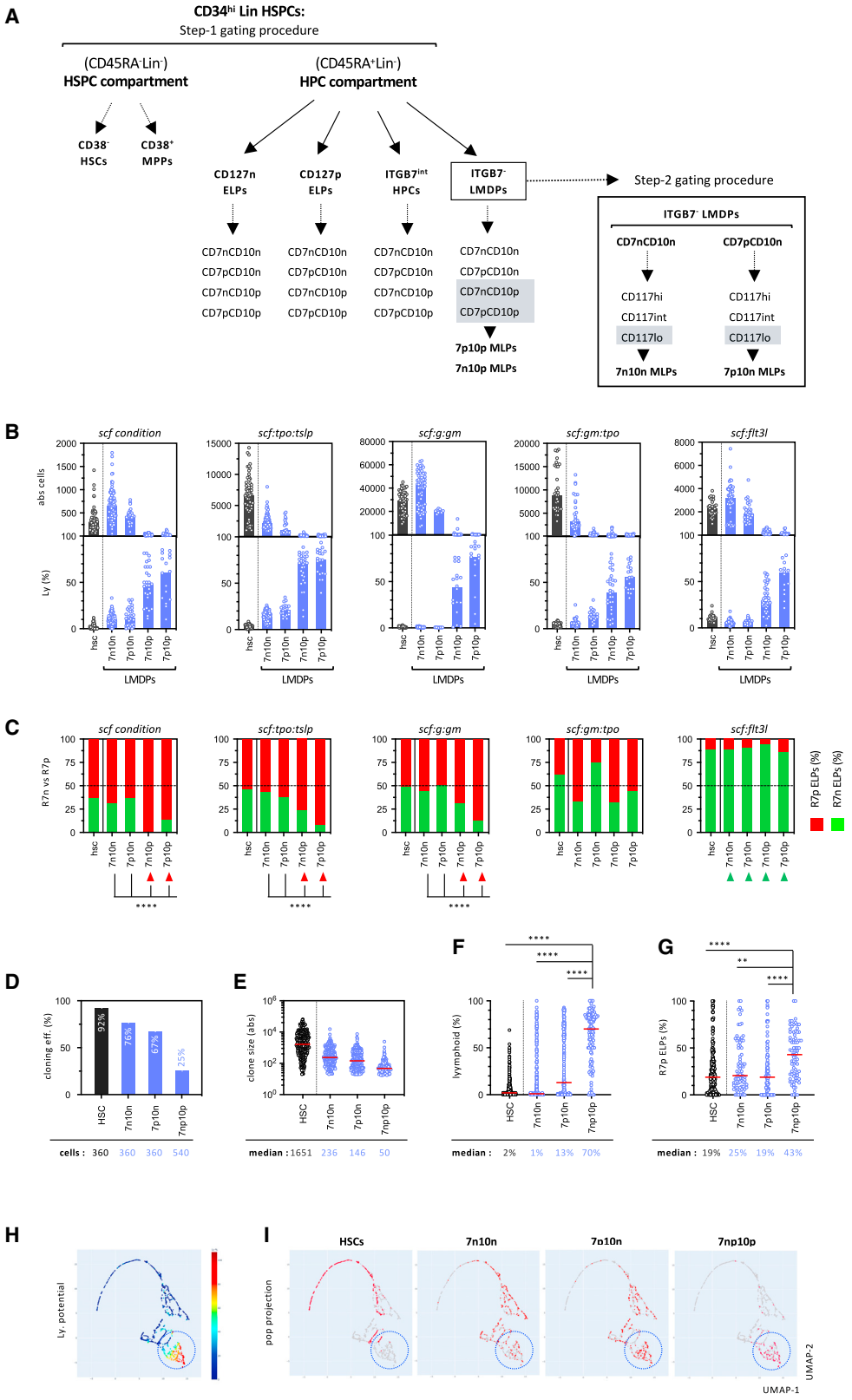

(legend on next page)

The search for ontogeny-related changes in lymphocyte production patterns in humans has long been hampered by limited characterization of lymphoid differentiation trajectories and controversies regarding the phenotype and function of lymphoid progenitors.[12] Since their identification,[13] extensive study of CD45RA$^+$CD10$^+$ multi-lymphoid progenitors (CD10$^+$ MLPs) has revealed that, despite an intrinsic B-lineage bias,[14] this population displays multi-lymphoid potential.[15,16] However, as CD10$^+$ MLPs are only detected after birth,[17,18] most current evidence suggests that fetal lymphopoiesis is supported by yet uncharacterized MLP subsets. Notably, a different population of CD45RA$^+$CD7$^+$ MLPs with robust T potential has been isolated from neonatal cord blood[19,20] but their developmental status remains poorly defined. We have previously shown that human lymphopoiesis displays a bipartite organization stemming from founder populations of CD127$^-$ and CD127$^+$ early lymphoid progenitors (ELPs) differentially polarized toward the natural killer (NK)/ILC/T or B lineages.[17] Searching for their origin revealed that CD127$^-$ and CD127$^+$ ELPs differentiate from prototypic MLPs and that they are subject to divergent Flt3L-inducible versus cell-autonomous regulation (Alhaj Hussen et al., submitted).

To explore the physiological implications of these findings and reconcile the bipartite model of lymphoid organization[17] with earlier studies that categorized lymphoid progenitors on the basis of differential CD7 and CD10 expression,[15] we subjected lymphoid progenitors from 140 blood and bone marrow (BM) donors between 13 weeks post-conception (PCW) and 87 years postnatal to a multi-modal characterization procedure. As well as showing that human lymphopoiesis is supported by sequential waves of embryonic, fetal, and postnatal MLPs, our data reveal that transition to postnatal life is associated with a B-lineage shift in the pattern of lymphocyte production.

RESULTS

Neonatal CD10$^+$ MLPs are intrinsically biased toward CD127$^+$ ELPs

To investigate the heterogeneity of lymphoid progenitors circulating in the umbilical cord blood (UCB), we developed optimized fluorescence-activated cell sorting (FACS) schemes of CD45RA$^+$Lin$^-$ hematopoietic progenitor cells (HPCs) by adding ITGB7 and CD127 to a previous six parameter design.[14,17] Neonatal CD45RA$^+$Lin$^-$ HPCs were first partitioned into four ITGB7$^-$ or ITGB7^{int} HPC and CD127$^-$ or CD127$^+$ ELP compartments, each of which was further subdivided according to differential CD7 and CD10 expression (Figures 1A and S1A–S1C [step 1 gating procedure]). Hereafter, ITGB7$^-$ HPCs are referred to as lympho-myelo-dendritic progenitors (LMDPs), following a previously established nomenclature.[17] Seeding the resulting 16 cellular fractions in B, NK/ILC, and T differentiation assays found the expected hotspots of lymphoid potential within CD127$^-$ and CD127$^+$ ELPs and confirmed that, among these, CD7 expression correlates with detection of NK/ILC/T potential (Figure S2). Also, consistent with our previous findings,[17] CD127$^+$ ELPs displayed robust B potential, irrespective of CD7 or CD10 expression.

As only marginal lymphoid potential was detected within the more immature LMDP and ITGB7^{int} compartments, we next investigated whether this was due to a lack of lymphoid competence or to the limited sensitivity of standard differentiation assays. To address this, LMDPs fractionated as above were seeded in multilineage diversification assays allowing simultaneous

Figure 1. CD10$^+$ MLPs are biased toward the CD127$^+$ ELPs

(A) List and nomenclature of 24 neonatal CD34$^+$ HSPCs subsets analyzed in this study. UCB CD34$^+$Lin$^-$ HSPCs were first subdivided into CD45RA$^-$ or CD45RA$^+$ compartments. Within CD45RA$^-$ compartment, CD38 expression levels distinguished HSCs from MPPs. In the step 1 gating procedure, the CD45RA$^+$ compartment was first partitioned into ITGB7$^-$ LMDPs, ITGB7^{int} HPCs, or CD127$^{-/+}$ ELPs (R7np), each of which being further subdivided into CD7 or CD10 negative (n) or positive (p) subsets. In the step 2 gating procedure, CD7$^-$CD10$^-$ and CD7$^+$CD10$^-$ LMDPs were further fractionated into CD117$^{hi/int/lo}$ subsets. Lymphoid-restricted CD117^{lo} subsets highlighted in gray are referred to as MLPs, in keeping with the current nomenclature. HSC, hematopoietic stem cell, MPP, multipotent progenitor; LMDP, lympho-myelo-dendritic cell progenitor; HPC, hematopoietic progenitor cell; ELP, early lymphoid progenitor; MLP, multi-lymphoid progenitor. The full gating procedure is presented in Figure S1.

(B and C) *In vitro* assessment of neonatal LMDP differentiation potentials in bulk diversification assays. (B) HSC (gray bars) or LMDPs (blue bars) subdivided on the basis of CD7 and CD10 expression (step 1 gating procedure) were seeded by 100-cell pools in 96-well plates and cultured for 10 days under the indicated conditions before quantification of *in vitro* differentiated myeloid granulocyte (Gr; CD15$^+$), monocyte (Mo; CD115$^+$), and dendritic cell (DC; CD123$^+$) precursors, or lymphoid CD127$^{-/+}$ ELPs and CD19$^+$ BL (see Figure S3A for the full gating procedure); bar plots show absolute cell numbers (upper panels) or percentages of lymphoid cells (lower panels); percentages of lymphoid cells are defined as the sum of the percentages of CD19$^+$ BL and CD127$^{-/+}$ ELPs; results are normalized relative to hu-CD45$^+$ cells; bars show median values; circles correspond to individual wells. Assessment of statistical significance by the Kruskal-Wallis test showed p values <0.0001 for all conditions. Quantification of myeloid output is provided as Figure S3B. (C) Stacked bar plots show the relative proportions of CD127$^-$ (green) and CD127$^+$ (red) ELPs. Results are expressed as median percentages from $\geq$10 individual wells; red and green arrows show polarized ELP production patterns. Assessment of statistical significance was performed using the Mann-Whitney test (CD7npCD10p versus others: ****p < 0.0001 by the Mann-Whitney test).

(D–G) *In vitro* assessment of neonatal LMDP differentiation potentials in clonal diversification assays. The indicated HSC or LMDP subsets were seeded individually in 96-well plates and cultured for 14 days onto OP9 stroma under the *scf:gm-csf:tpo* condition before quantification of lympho-myeloid output (see Figure S3C for the gating procedure). Positivity threshold for clone detection was se arbitrarily at $\geq$20 cells/clone. Bar and circle plots show (D) cloning efficiencies, (E) absolute cell numbers per individual clone, (F) total lymphoid output or (G) relative percentages of CD127$^+$ ELPs within each clone normalized relative to total ELPs (positivity threshold for ELP detection was set arbitrarily at $\geq$10 ELPs/clone). For circles plots, red bars show the medians. Corresponding values are indicated below each plot. Note that because of overall similar cloning efficiencies and lymphoid potentials results obtained with CD7$^-$CD10$^+$ and CD7$^+$CD10$^+$ MLPs were pooled. Assessment of statistical significance was performed using the Mann-Whitney test **p < 0.01, ***p < 0.001, and ****p < 0.0001).

(H and I) Bidimensional projection into a uniform manifold approximation and projection (UMAP) of lymphoid-containing clones. The UMAP algorithm was applied to the data pooled from all experiments and ancestor cell types (n = 2,633) with each ancestor cell being projected into the UMAP coordinates. (H) Heatmap shows lymphoid potentials defined as percentages of lymphoid cells per clone across all ancestor cells. (I) Snapshots show projection of clones derived from the indicated subsets; dashed circles indicate lymphoid-enriched area. Results are pooled from 5 independent experiments.

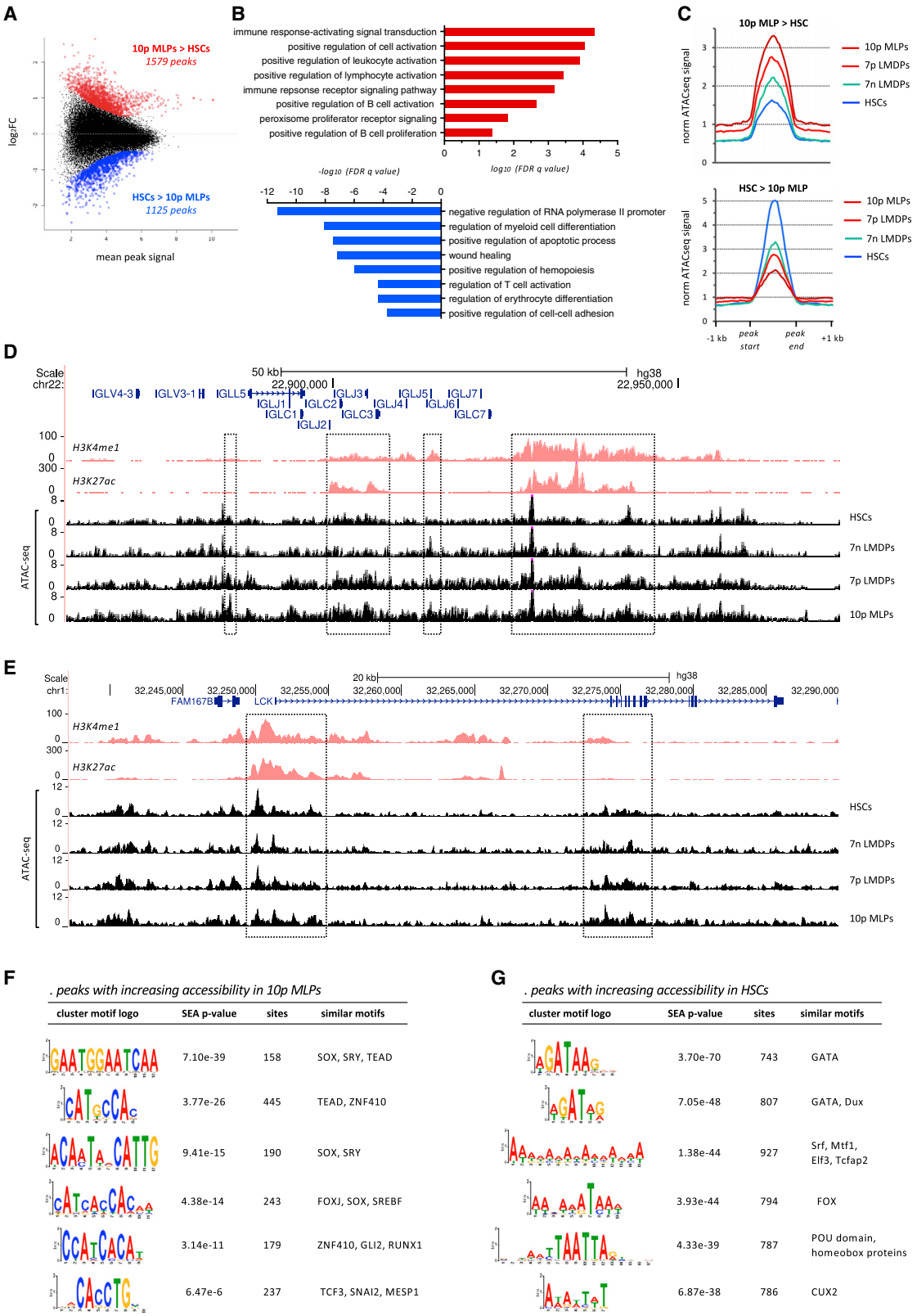

F

. peaks with increasing accessibility in 10p MLPs

cluster motif logo	SEA p-value	sites	similar motifs
	7.10e-39	158	SOX, SRY, TEAD
	3.77e-26	445	TEAD, ZNF410
	9.41e-15	190	SOX, SRY
	4.38e-14	243	FOXJ, SOX, SREBF
	3.14e-11	179	ZNF410, GLI2, RUNX1
	6.47e-6	237	TCF3, SNAI2, MESP1

G

. peaks with increasing accessibility in HSCs

cluster motif logo	SEA p-value	sites	similar motifs
	3.70e-70	743	GATA
	7.05e-48	807	GATA, Dux
	1.38e-44	927	Srf, Mtf1, Elf3, Tcfap2
	3.93e-44	794	FOX
	4.33e-39	787	POU domain, homeobox proteins
	6.87e-38	786	CUX2

(legend on next page)

generation of granulomonocytic, dendritic, and lymphoid precursors (Figure S3A). Cultures were supplemented with *scf* only or with cytokine cocktails optimized for lymphoid (*scf:tpo:tslp*), multilineage (*scf:flt3l* or *scf:gm:tpo*) or myeloid (*scf:g:gm*) differentiation. Consistent with an earlier report,[15] the CD10$^+$ fractions expanded poorly and generated a majority of lymphoid cells (Figures 1B and S3C). Except for the *scf:flt3l* condition that induced a complete lymphoid shift toward CD127$^-$ ELPs, the CD10$^+$ fractions were markedly biased toward the CD127$^+$ ELPs, with no consistent difference being noted with respect to CD7 co-expression (Figure 1C). This contrasts with their CD10$^-$ counterparts that expanded robustly, showed mixed lympho-myeloid potentials, and displayed balanced CD127$^-$ and CD127$^+$ ELP output. Single-cell differentiation assays (Figure S3B) confirmed that the CD10$^+$ fractions have reduced cloning efficiency, undergo limited expansion and that they mostly generate lymphoid cells with a high proportion of CD127$^+$ ELPs (Figures 1D–1I and S3D–S3F). In contrast, their CD10$^-$ counterparts proved highly heterogeneous including multipotent as well as already myeloid or lymphoid lineage-specified progenitors with, here again, balanced lymphoid output.

These data confirm that expression of CD10 by neonatal LMDPs is indicative of lymphoid specification and an intrinsic differentiation bias toward the generation of CD127$^+$ ELPs. In keeping with the current nomenclature,[15] CD10$^+$ LMDPs are hereafter referred to as CD10$^+$ MLPs.

Neonatal CD10$^+$ MLPs are epigenetically primed toward the B lineage

To investigate the molecular events underlying intrinsic B-lineage bias of neonatal CD10$^+$ MLPs, we carried out assay for transposase-accessible chromatin with sequencing (ATAC-seq) experiments to compare their chromatin accessibility profile with that of HSCs and of CD7$^-$CD10$^-$ and CD7$^+$CD10$^-$ LMDPs (Figure S4A). Consistent with recent findings that HSCs exhibit a generally open chromatin structure,[21] the highest number of peaks was observed in HSCs (40,763 peaks, false discovery rate [FDR] < 0.05). Peak number decreased progressively in CD7$^-$CD10$^-$ (35,457 peaks) and CD7$^+$CD10$^-$ LMDPs (26,910 peaks), and the lowest number of peaks was detected in CD10$^+$ MLPs (19,291 peaks) consistent with a gradual extinction of alternative lineage potentials during lymphoid specification (Figure S4B). Subsequent analysis was carried out on a master set of 46,531 peaks, composed of all peaks present in at least one population. To establish the profile of chromatin changes associated with lymphoid commitment, we initially compared the accessibility at these peaks between HSCs and CD10$^+$ MLPs and identified 1,579 peaks with increased accessibility and 1,125 peaks with decreased accessibility (FDR q < 0.05, $\log_2$ fold change [FC] > 0.5) during lymphoid commitment (Figure 2A). Relative to the complete peak set, peaks which change during lymphoid commitment are enriched at intronic and gene-distal sites (Figure S4C), consistent with previous findings that hematopoietic lineage commitment is primarily dictated by gene-distal enhancer elements.[22] Genes associated with peaks of increasing accessibility in CD10$^+$ MLPs were enriched for pathways of immune receptor signaling, B cell activation and expansion, confirming their lymphoid-committed status and B-lineage bias (Figure 2B; Table S1). In contrast, genes associated with sites of decreasing accessibility were enriched for general cellular processes (transcription, apoptosis, and cell adhesion) as well as the regulation of myeloid, T lymphoid, and erythroid pathways. Pileup analysis of accumulated ATAC signal confirmed that these changes are partially detected in CD7$^-$CD10$^-$ LMDPs and increase further in CD7$^+$CD10$^-$ LMDPs (Figures 2C, S4D, and S4E). Representative examples of gradually acquired accessibility at regulatory elements associated with lymphoid genes (IGL, LCK, TNFAIP3) and their gradual decline at genes important for alternative cell fates (e.g., the erythroid-determining factor NFE2) are shown (Figures 2D, 2E, S4F, and S4G). Consistent with these results, analysis of DNA motifs in regions of increased accessibility in CD10$^+$ MLPs revealed strong enrichment for motifs recognized by the B-lymphoid transcription factors (TFs) SOX4, TEAD1/TEF1, and TCF3,[23] while peaks of decreasing accessibility were most enriched for motifs recognized by the GATA family of TFs (Figures 2F and 2G).

These results confirm that CD10$^+$ MLPs are epigenetically primed toward the B lineage and demonstrate that the molecular changes associated with lymphoid specification are progressively acquired.

Functionally distinct MLP subsets circulate in neonatal blood

We have recently shown that the lymphoid potential of fetal MLPs can be defined on the basis of low CD117 expression

Figure 2. CD10$^+$ MLPs are epigenetically primed toward the B lineage

(A) Mean difference (MD) plot of 46,531 total ATAC-seq peaks showing $\log_2$(fold change) of ATAC-seq peak signal in CD10$^+$ (10p) MLPs relative to signal in HSCs against mean signal of each peak; peaks increasing (FDR q < 0.05, $\log_2$FC > 0.5) or decreasing (FDR q < 0.05, $\log_2$FC < −0.5) in CD10$^+$ MLPs relative to HSCs are indicated in red (1,579 peaks) and blue (1,125 peaks), respectively.

(B) Selected Gene Ontology (GO) (Biological Process) categories enriched (FDR q < 0.05) in genes associated with peaks of increased (cayenne) or decreased (blue) accessibility in CD10$^+$ MLPs relative to HSCs. The full list of enriched categories is provided in Table S1.

(C) Cumulative normalized ATAC-seq signal at peaks increasing (1,579 peaks; top panel) or decreasing (1,125 peaks; bottom panel) in CD10$^+$ MLPs relative to HSCs; shown is the mean cumulative signal observed at these peak sets in the indicated populations.

(D and E) University of California, Santa Cruz (UCSC), Genome Browser snapshots showing changes in chromatin accessibility observed in the indicated populations at *cis*-elements within the (D) IG lambda and (E) LCK loci (from GO category: immune response-activating signal transduction); gene annotation (GENCODE V38) is shown at top followed by Encode tracks demonstrating enhancer-associated histone modifications (H3K4me1 and H3K27ac) in the GM12878 lymphoblastoid cell line. Regions whose accessibility increases during lymphoid specification are highlighted (dashed boxes).

(F and G) Results of motif enrichment analysis (XSTREME) showing the 6 most enriched motif clusters detected in peaks of increased accessibility in (F) 10p MLPs or (G) HSCs; shown for each cluster is the significance of enrichment (simple enrichment analysis E value), the number of times that the motif is detected in the test peak set (sites), and similar known motifs detected in the TomTom dataset. 10p, CD10$^+$CD7$^-$; 7p, CD10$^-$CD7$^+$; 7n, CD10$^-$CD7$^-$.

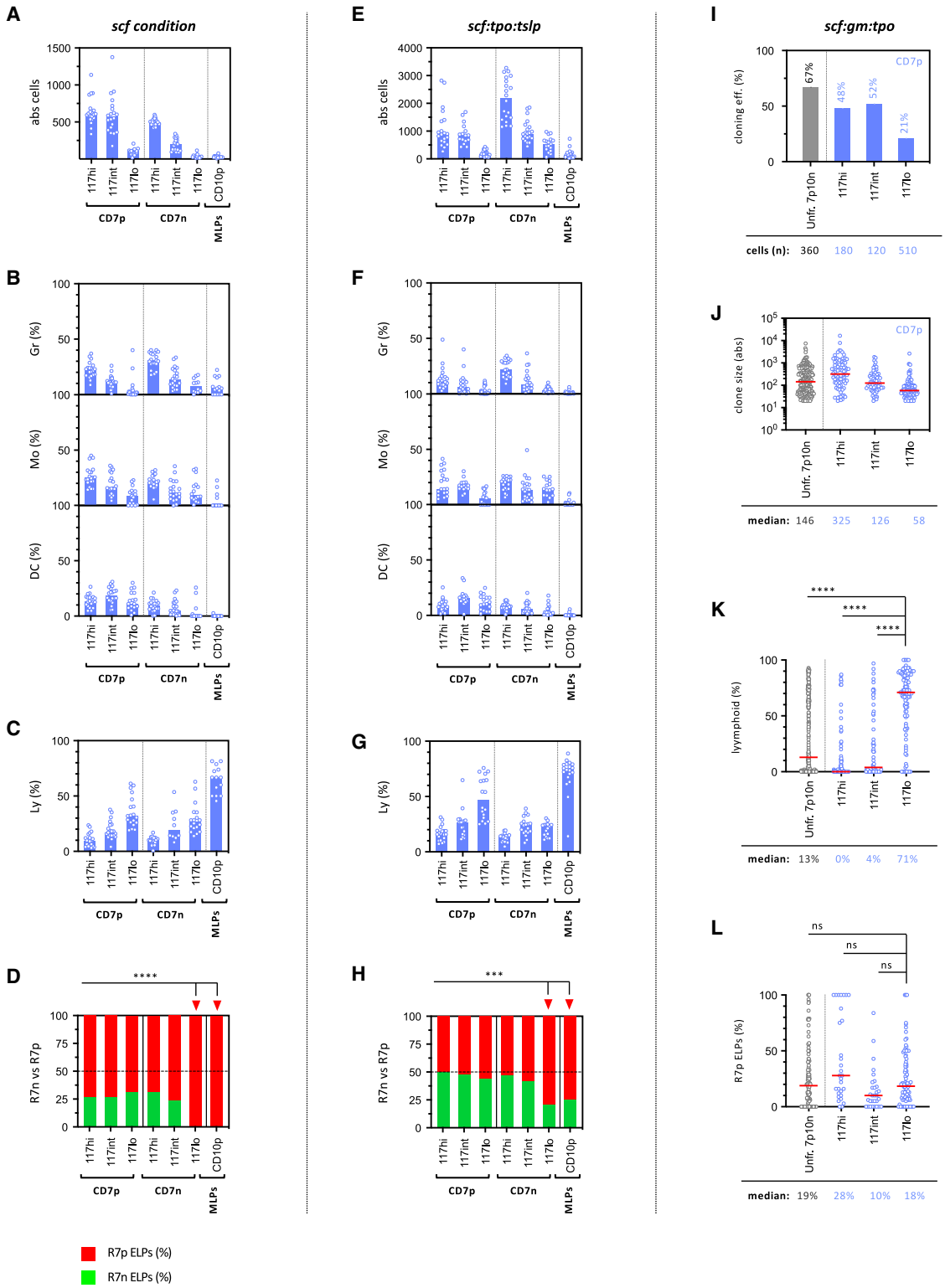

Figure 3. Functional characterization of neonatal MLPs

(A–H) Functional characterization of CD117$^{hi/int/lo}$ LMDP subfractions in bulk diversification assays. CD7^{-} or CD7^{+} LMDPs were partitioned into CD117$^{hi/int/lo}$ fractions (Figure S1C: step 2 gating procedure) and seeded as above under the (A–D) *scf* or (E and H) *scf:tpo:tslp* conditions before quantification of cell growth and lineage output (see also legends of Figures 1B and 1C). Bar plots show (A and E) absolute cell numbers; (B and F) percentages of myeloid granulocyte (upper

(legend continued on next page)

(Alhaj Hussen et al., submitted). To determine whether this also applies to their neonatal counterparts, cord blood CD7$^{-/+}$CD10$^{-/+}$ LMDP subsets were stratified according to CD117 levels (Figure S1C [step 2 gating procedure]). As expected, we found that CD10^{+} MLPs express uniformly low levels of CD117. Since CD7^{+} or CD7^{-} LMDPs express variable levels of CD117, they were further fractioned on this basis and seeded as above in diversification assays. Culture under *scf* (Figures 3A–3D) or *scf:tpo:tslp* (Figures 3E–3H) conditions confirmed that downmodulation of CD117 coincides here again with reduced proliferation, decreasing myeloid potential and a corresponding increase in the lymphoid output. Furthermore, analysis of ELP production patterns revealed that, conversely to their CD7^{-} or CD10^{+} counterparts that are markedly biased toward CD127^{+} ELPs, the CD117^{lo}CD7^{+} LMDPs give rise to both CD127^{-} and CD127^{+} ELP output (Figures 3D and 3H). Single-cell cultures confirmed that CD117^{lo}CD7^{+} LMDPs display limited cloning efficiency and reduced expansion and mostly generate lymphoid cells among which CD127^{-} ELPs predominate (Figures 3–3L). Collectively, these data indicate that distinct subsets of CD7^{+}CD10^{-}, CD7^{-}CD10^{-}, and CD7$^{-/+}$CD10^{+} MLPs with balanced or B lineage-biased lymphoid differentiation potentials circulate in the neonatal cord blood.

Neonatal MLPs display overlapping gene signatures

To characterize the changes in gene expression associated with lymphoid specification and search for transcriptional correlates of the differences in the pattern of ELP production observed between CD7$^{-/+}$CD10$^{-/+}$ MLPs, 11 neonatal hematopoietic stem cell progenitor (HSPC) populations were subjected to transcriptional profiling using ultra-low-input mini-RNA sequencing (Figure 4A). Principal-component analysis (PCA) showed co-clustering of all MLP subsets and confirmed that downstream CD127^{+} ELPs are more distantly related (Figure 4B). Within CD117$^{int/hi}$ LMDPs, PCA also allowed distinction between the CD7^{-} and CD7^{+} cell fractions, with the latter overexpressing Notch target genes (*HES1*, *FBXW5*, and *CDCA7*) (data not shown).

A total of 55 pairwise comparisons between the indicated subsets identified 1,773 differentially expressed genes (DEGs) distributed in 10 clusters (P1–P10) (Tables S2A–S2C). Functional analysis of gene enrichment patterns and cluster distribution recapitulated the hematopoietic hierarchy with the most immature CD38^{-} or CD38^{+}CD45RA^{-} subsets overexpressing genes involved in stem cell maintenance (P1: *FLT1*, *HOXB2*, *TAL1*, and *HHEX*) and/or early hematopoietic differentiation (P2: *GATA2*, *SPI1*, *TIE1*, *CSF2RB*, and *CXCR4*) (Figure 4C). Consistent with granulomonocytic specification, CD117^{hi} LMDPs upregulated *CSF3R*, *CEBPA*, *LYZ*, *MPO*, *CTSG*, and *CTSW* transcripts (P3–P5). As expected, onset of lymphoid priming was detected within the CD117^{int} LMDP fractions (P6–P7) and coincided with overexpression of Notch target genes *HES1* or *HES4*, acquisition of *IL21R* and upregulation of TFs controlling early lymphoid specification (*IKZF1*, *BCL11A*, and *ZBTB1*) or dendritic cell differentiation (*IRF8*). A second wave of lymphoid TFs (*ETS1*, *RUNX3*, *TCF3*, *SOX4*, and *ZBTB7A*) was detected in downstream CD117^{lo} MLPs (P8). Gene expression in CD117^{lo} MLPs was similar irrespective of CD7 or CD10 expression. Finally, consistent with a more advanced differentiation status, the highest expression levels of *IRF1*, *ID2*, *TCF4*, and *Notch3*, as well as of BCR components (*CD22*, *CD79A*, *CD79B*, and *LAT2*) were detected in CD127^{+} ELPs (P9), that no longer expressed stem/progenitor cell-associated TFs (*LYL1*, *MEIS1*) or myeloid lineage (*STAT3*, *CEBPB*, *CEBPG*, *GFI1B*, *IL3RA*, and *IL6R*) genes (P10).

Regulatory network analysis including TFs upregulated in neonatal MLPs (P6–P8) and their potential target genes (Figure S5A) confirmed the role played by MEF2-family TFs during lymphoid specification.[24] This also revealed three additional densely connected nodes represented by the HOX-family tumor suppressor CUX1,[25] as well as by the TFEB activator of lysosomal activity[26] and the FOXN3 cell-cycle regulator,[27] which suggests that following egress into the blood, these MLPs upregulate a quiescence program.

In conclusion, these results show that, irrespective of CD7 or CD10 expression, neonatal MLPs display overlapping lymphoid transcriptional signatures, consistent with the idea that the differences in ELP production pattern reported above are conditioned at the epigenetic level.

Differential CD7 and CD10 expression identifies embryonic, fetal, and postnatal MLPs

Inasmuch as earlier studies provided evidence that CD7 is expressed preferentially during the fetal period,[19,28] we next hypothesized that rare CD7^{+} MLPs circulating in the neonatal blood could have an embryonic or fetal origin. To address this question, BM CD34^{+} HSPCs from 14 fetal (13–23 PCW) and 50 postnatal (2–87 years) donors were subjected to optimized immunophenotypic profiling. As well as showing a predominance of monocyte and dendritic precursors in the BM of fetal donors before 16 PCW (data not shown), these analyses found that lymphoid progenitors reach maximum levels by 18–20 PCW and remain at stable levels until puberty, after which they gradually decline to represent $\leq$3% of total HSPCs after 60 years (Figure 5A). Further dissection of lymphoid architecture revealed that whereas CD127^{-} and CD127^{+} ELPs are produced in comparable amounts

panel), monocyte (medium panel), or dendritic (lower panel) precursors; (C and G) percentages of lymphoid cells. Bars indicate medians; circles correspond to individual wells; assessment of statistical significance was performed using the Kruskal-Wallis test (****$p < 0.0001$ for all conditions). Stacked bar plot shows (D and H) the relative proportions of CD127^{-} (green) and CD127^{+} (red) ELPs; results are expressed as median percentages from $\geq$10 individual wells; red arrows show statistically significant differences (CD117^{lo}CD7^{-}10^{-} or CD10^{+} versus others; ****$p < 0.0001$ by the Mann-Whitney test).

(I–L) Clonal diversification assays. CD7^{+} LMDPs fractioned as above on the basis of CD117 expression levels were seeded individually in 96-well plates and cultured for 14 days onto OP9 stroma before quantification of lineage outputs. Bar and circle plots show: (I) cloning efficiencies; (J) absolute cell number per clone (clone size); percentages of (K) total lymphoid cells or (L) CD127^{+} ELPs per clone. CD127^{+} ELP percentages are normalized relative to total ELPs. For circles plots, red bars correspond to the median values shown below each plot; assessment of statistical significance was performed using the Mann-Whitney test (**$p < 0.01$, ***$p < 0.001$, and ****$p < 0.0001$). Results are pooled from 3 experiments.

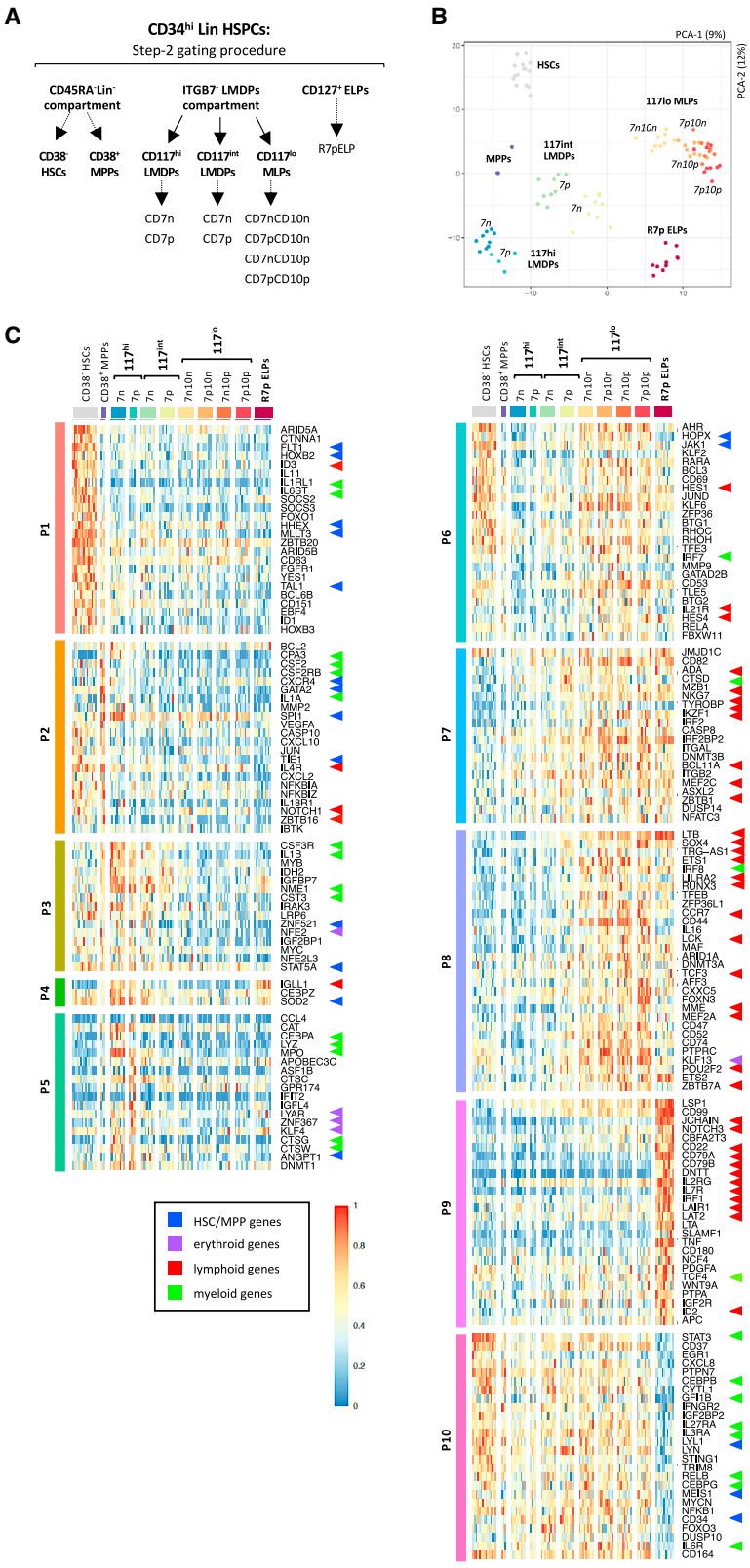

Figure 4. Transcriptional profiling of neonatal MLPs

(A) List and nomenclature of 11 neonatal CD34$^+$ HSPCs subsets analyzed by mini-RNA-seq. The indicated lineage-negative (Lin$^-$) CD45RA$^-$ or CD45RA$^+$ fractions were sorted from freshly isolated UCB CD34$^+$ HSPCs, cultured for 3 h in cytokine-supplemented medium (*scf:gm:tpo*), and sorted again by 100 cell batches (3–9 replicates/population) before being processed for mini-RNA-seq.

(B) Principal-component analyses (PCAs) of transcriptome data.

(C) Heatmaps showing expression of 209 selected DEGs across 10 clusters (P1–P10). Gene expression values are log-transformed, normalized, and scaled; colored arrows show lineage- or subset-specific genes. See also Tables S2A–S2C for the distribution of the 1,773 DEGs within clusters P1–P10.

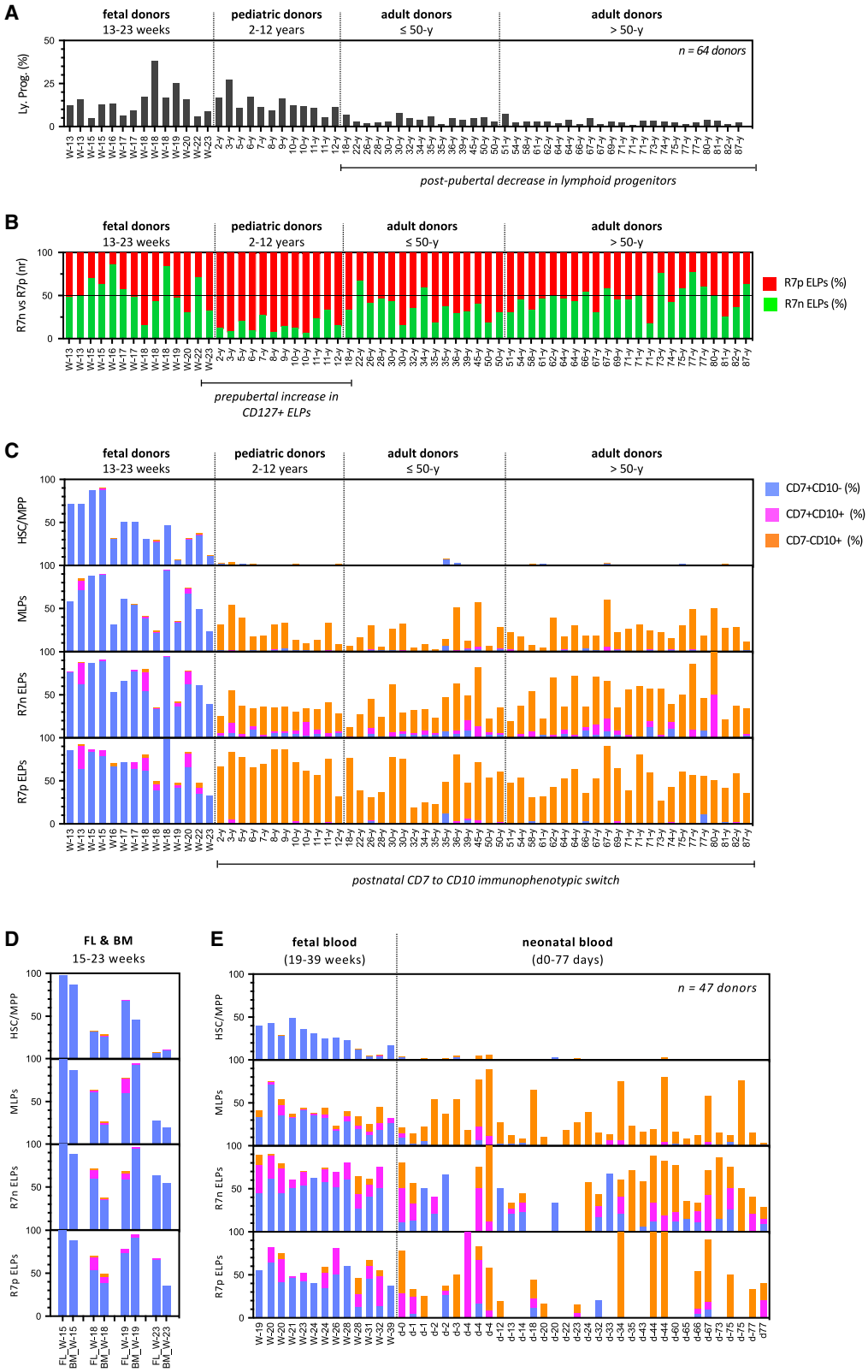

(legend on next page)

throughout the fetal period, a clear bias toward CD127$^+$ ELPs is observed immediately after birth and persists until puberty (Figure 5B). Subsequent assessment of CD7 and CD10 expression showed that whereas early in development FL and BM CD34$^+$ HSPCs, including most immature CD45RA$^-$CD38^{lo} HSC/MPPs (Figure S1D) homogeneously express CD7, beyond the first trimester of gestation percentages of CD7$^+$ HSPCs gradually decline until birth (Figures 5C and 5D). Despite restriction to the lymphoid lineage, the pattern of expression of CD10 also showed ontogeny-related variations. In contrast to the fetal period where it remains confined to the CD24$^+$CD19$^{-/+}$ B cell compartment,[17,18] after birth the expression of CD10 is acquired as early as the stage of MLPs (median 20%, range 3%–50%, n = 52, age 2–87 years) (Figure S1E). Further immunophenotypic profiling of CD34$^+$ HSPCs in the blood of 47 fetal or neonatal donors between 19 PCW and 77 day postnatal confirmed that the immunophenotypic switch from CD7 to CD10 on lymphoid progenitors takes place within the first few days after birth (Figure 5E).

Collectively, these results show that the transition to postnatal life coincides with a global B-lineage shift in lymphopoiesis characterized by a prepubertal increase in the production of CD127$^+$ ELPs accompanied by an immunophenotypic CD7 to CD10 conversion of lymphoid progenitors which takes place around birth and is maintained throughout postnatal life. On the basis of these data, CD7$^+$CD10$^-$, CD7$^-$CD10$^-$, and CD7$^-$CD10$^+$ MLPs are subsequently referred to as embryonic, fetal, and postnatal MLPs, respectively.

Fetal lymphoid progenitors retain expression of myeloid lineage genes

To search for ontogeny-related changes in lymphoid transcriptional signatures, mini-RNA sequencing was performed on 14 HSPC subsets from 2 fetal (19–20 PCW) and 4 postnatal (15–52 years) BM donors (Figures S6A and S6B). Consistent with a previous report,[29] global comparison between fetal and postnatal CD34$^+$ HSPC subsets (1,034 DEGs) showed *LIN28B* overexpression and enrichment of cell-cycle, protein synthesis, and oxidative phosphorylation pathways in the fetal subsets versus stress- or inflammatory-response pathways in their postnatal counterparts (Figure S5C; Tables S3A–S3C).

Transcriptional profiling of fetal HSPCs identified 517 DEGs distributed in 8 clusters (P1–P8) (Figure S6C; Tables S4A–S4C). Consistent with a more primitive developmental status, gene enrichment analyses revealed that the CD7$^+$ HSCs (CD45RA$^-$CD38$^-$) are enriched with genes involved in stem cell activation/proliferation (*MYCN*, *GATA1*, *GATA2*, and *ZBTB16*) and eosinophil/basophil or mast cell differentiation (*LMO4*, *IKZF2*, *CPA3*, *HDC*) (P1), while their CD7$^-$ counterparts upregulate markers of postnatal HSCs (*ITGA6/CD49F*, *Prom1/CD133*) and regulators of stem cell self-renewal (*HLF*, *HOPX*, *MEIS1*, *MLLT3*, *HOXB3*, and *SOD2*) (P2). Despite these differences, CD7$^+$ and CD7$^-$ HSCs shared expression of genes involved in multilineage priming (*VENTX*, *MECOM*, *ARID3B*, *ARID4A*, and *POU2F1*) and erythroid (*TAL1* and *NFE2*) or myeloid (*CSF3R* and *IL1B*) differentiation (P3). Downstream CD7$^+$CD117^{hi} HPCs unexpectedly showed enrichment in genes involved in lung, kidney, cardiovascular, or brain development (*HOXA5*, *NPHP3*, and *VAX1*) (P4), and shared with their CD7$^-$ counterparts expression of granulocyte genes (P5: *CEBPA*, *MPO*, and *ELANE*). These analyses also showed that, in contrast to their neonatal counterparts, fetal MLPs display a composite gene signature characterized by combined enrichment in monocyte/dendritic (*CSF1R*, *IRF8*, *MPEG1*, and *SAMHD1*) and lymphoid (*LTB*, *CD2*, *ID3*, *IL7R*, *BLNK*, and *VPREB1/3*) lineage genes, the latter's being further upregulated in downstream CD127$^-$ or CD127$^+$ ELPs (P6–P8). Again, no difference in gene expression was noted between CD7$^-$ or CD7$^+$ MLP subfractions.

Gene enrichment and functional analyses of adult CD34$^+$ HSPCs (339 DEGs; Figure S6D; Tables S5A–S5C) confirmed overexpression of genes associated with stress inflammatory response (*JUN*, *NFE2L2*, *IL1B*, and *EGR1*) and resistance to apoptosis (*AVP*, *CLU*, HSBP1, and *PRDX1*) in the HSC compartment (Q1–Q2) and found the expected granulocyte (Q3) or monocyte/dendritic (Q4–Q5) gene signatures within CD117^{hi} and CD117^{int} LMDPs. In contrast to their fetal counterparts, adult CD117^{lo}CD10$^-$ MLPs downregulated most myeloid genes while showing limited evidence of lymphoid priming that became obvious only in CD10$^+$ MLPs. Here again, CD10$^+$ MLPs and CD127$^+$ ELPs displayed the expected multi-lymphoid (*TYROBP*, *MEF2A/C*, *SATB1*, *SOX4*, and *CCR7/9*) (Q6) or B lineage-biased gene signatures (Q7). Subsequent regulatory network analysis of the TFs and their potential target genes overexpressed by fetal and postnatal MLPs (Figure S5B) disclosed 2 densely connected nodes corresponding to SATB1[30] and MEF2-family TFs,[24] an indication that their role in lymphoid specification is conserved across ontogeny.

Collectively, these data show that, conversely to their postnatal counterparts, proliferating fetal lymphoid progenitors retain expression of monocyte or dendritic lineage genes. Furthermore, they indicate that in the adult BM lymphoid commitment coincides with CD10 upregulation.

Figure 5. Transition to postnatal life coincides with a B-lineage shift of lymphopoiesis

(A) Dynamics of lymphoid progenitors in the BM of 14 fetal and 50 postnatal donors. Gates were set as described in Figure S7 (gating strategy 1); results are normalized according to total CD34^{hi}Lin$^-$ HSPCs.

(B) Stacked bar plots show the relative proportions of BM CD127$^-$ (green) and CD127$^+$ (red) ELPs in the same donors; results are normalized relative to total ELPs.

(C) Stacked bar plots show age-dependent variations in CD7 or CD10 expression across HSC, MLP, CD127$^-$ or CD127$^+$ ELP compartments in the same BM donors; results are expressed as relative percentages within each subset.

(D) Stacked bar plots show comparative expression of CD7 and CD10 by fetal liver (FL) or BM CD34$^+$ HSPCs from the same 4 donors between 15 and 23 development weeks; gates were set as described above; results are expressed as relative percentages of CD7- or CD10-expressing cells within the indicated cellular subsets.

(E) Stacked bar plots show age-dependent variations in CD7 and CD10 expression by CD34$^+$ HSPCs circulating in the blood of 47 donors between 19 PCW and 77 days postnatal.

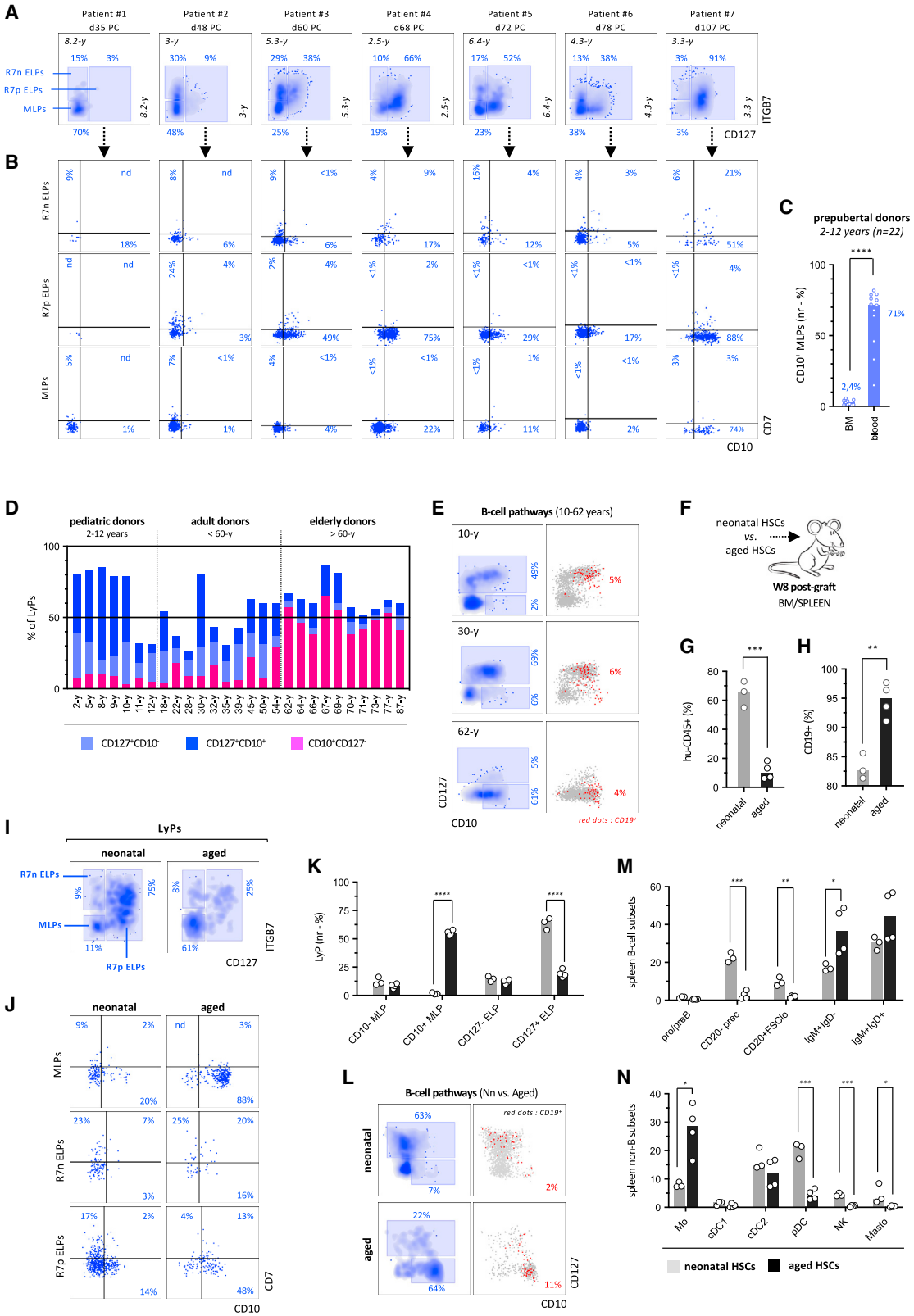

(legend on next page)

CD10$^+$ MLPs circulate in high numbers in the blood of prepubertal donors

To further investigate the developmental status and biological function of postnatal CD10$^+$ MLPs, we next monitored lymphoid regeneration in 7 pediatric patients (2–8 years) between 35 and 107 days after treatment by chemotherapy for acute lymphoblastic or myeloblastic leukemia. Immunophenotypic profiling of lymphoid progenitors in these patients found that CD127$^-$ and CD127$^+$ ELPs emerge sequentially within the first two months after treatment with the latter appearing to accumulate throughout the regenerative period (Figure 6A). These analyses also revealed that only a minority of newly produced ELPs express CD7 which confirms that even under regenerative conditions postnatal HSCs have a decreased capacity to enter the NK/ILC/T differentiation pathway (Figure 6B). We also found that from the second month after chemotherapy, a large proportion of newly produced CD127$^+$ ELPs upregulate CD10, indicating their progression along the B cell differentiation pathway. However, to our surprise, within the first three months of chemotherapy, only rare CD10$^+$ MLPs were detected in the BM of these patients. Normal levels of CD10$^+$ MLPs were only observed around day 100 post-chemotherapy. As well as indicating that under regenerative conditions CD10$^+$ MLPs are late products of lymphoid diversification, these data show that they are not obligatory precursors of CD127$^-$ and CD127$^+$ ELPs after birth. As CD10$^+$ MLPs account for the majority of lymphoid progenitors in neonatal cord blood (Figure S1F) and have been proposed as postnatal thymus colonizers,[31,32] we next compared their distribution between blood and BM compartments in 22 pediatric donors between 2 and 12 years (Figure 6C). These analyses revealed that percentages of CD10$^+$ MLPs are 30-fold higher in blood than BM indicating that during the prepubertal period these MLPs display a selective capacity to enter the circulation to possibly reach the thymus or secondary lymphoid organs.

Altogether, these results indicate that immediately after birth and throughout the prepubertal period lymphoid architecture is characterized by a functional tripartition between CD127$^-$ and CD127$^+$ ELPs and circulating CD10$^+$ MLPs. They also suggest that before puberty CD10$^+$ MLPs contribute only marginally to BM lymphopoiesis.

Identification of a direct CD10$^+$ MLP-based B cell differentiation pathway in the elderly

To further investigate the developmental relationships between CD10$^+$ MLPs and CD127$^+$ ELPs, lymphoid progenitors from 27 donors between 2 and 87 years were subjected to optimized immunophenotypic fractionation. This showed that whereas CD127$^+$ ELPs largely predominate during the first five decades of life, CD10$^+$ MLPs become the major lymphoid-progenitor subset after 60 years of age, thus arguing for a late shift in B cell differentiation pathways (Figure 6D). Subsequent mapping of B cell differentiation trajectories confirmed that in younger donors CD127$^+$ ELPs emerge from the CD10$^-$ MLPs and sequentially upregulate CD10 and CD19 (Figure 6E). This contrasted with elderly donors in which B cell differentiation stems directly from CD10$^+$ MLPs, largely bypassing the CD127$^+$ ELPs.

To examine whether this late transition in the B-lineage differentiation paths is developmentally imprinted, NOD-*Scid*-*IL2rg*^{null} (NSG) mice were transplanted with CD45RA$^-$CD38^{lo} HSCs isolated from the BM of 65- and 80-year-old healthy donors and sacrificed two months later (Figure 6F). As expected, this found that hu-CD45$^+$ cells represented $\leq$10% of BM cells in mice

Figure 6. Age-related changes in B cell differentiation pathways

(A and B) Immunophenotypic profiling of lymphoid progenitors in the BM of pediatric patients (2.5–8.2 years) between 35 and 107 days after treatment for acute myeloblastic leukemia (AML) or acute lymphoblastic leukemia (ALL). Gates were set as described in Figure S7 (gating strategy 2). (A) Upper density plots show the subdivision of lymphoid progenitors into MLP, CD127$^-$, or CD127$^+$ ELP subsets; (B) lower dot plots show the expression of CD7 and CD10 by the corresponding subsets. Percentages are indicated.

(C) Quantification of blood and BM CD10$^+$ MLPs in 22 pediatric donors (blood, n = 12; BM, n = 10) between 2 and 12 years. Results are normalized relative to total CD34$^+$CD45RA$^+$Lin$^-$ HPCs. Bars indicate medians; circles correspond to individual donors; assessment of statistical significance was performed using the Mann-Whitney test (****p < 0.0001 for all conditions).

(D and E) Dynamics of BM CD10$^+$ MLPs and CD127$^+$ ELPs in postnatal BM. (D) Quantification of BM CD127$^{-/+}$CD10$^{-/+}$ HPCs in 27 postnatal donors between 2 and 87 years; stacked bar plot show percentages of the indicated subsets; gates were set as described in Figure S7 (gating strategy 3). (E) Immunophenotypic mapping of B cell differentiation pathways in 3 representative BM donors. Upper density plots showing age-related changes in BM CD10$^+$ MLPs and CD127$^+$ ELPs; lower dot plots overlays show projection of CD19$^+$ cells within the corresponding subsets; percentages are indicated.

(F–L) *In vivo* assessment of age-related changes in HSC lymphoid potential. (F) Experimental design: NSG mice reconstituted with 2.5 × 10^5 HSCs from two donors aged 65 and 80 years (2 mice/donor) or from the UCB (n = 3) were sacrificed 8 weeks after grafting. Immunophenotypic profiling of hu-CD45$^+$ BM and spleen cells was performed by spectral cytometry using a 35 antibody panel. (G and H) Bar plots show percentages of (G) hu-CD45$^+$ cells (normalized relative to total BM mononuclear cells) or (H) CD19$^+$ B lymphocytes (normalized relative to hu-CD45$^+$ cells) in mice reconstituted with neonatal or aged HSCs. (I–L) Immunophenotypic profiling of BM lymphoid progenitors; (I) upper density plots show the subdivision of lymphoid progenitors into MLP and CD127$^-$ or CD127$^+$ ELP subsets; (J) lower dot plots show CD7 and CD10 expression; percentages of the corresponding subsets are indicated; FACS data are pooled from 3 (nnHSCs) or 4 (aHSCs) xenografted mice; (K) bar plot showing percentages the indicated subsets (normalized relative to total lymphoid progenitors) (see also Figure S6: gating strategy 1); circles correspond to individual mice; bars indicate medians; assessment of statistical significance is based on the unpaired t test (**p < 0.01 and ***p < 0.001); gates are set on the CD34$^+$Lin$^-$CD45RA$^+$CD117^{lo} Ly compartment; (L) immunophenotypic mapping of B cell differentiation pathways in the same xenografted mice; left density plots showing ontogeny-related changes in CD10$^+$ MLPs and CD127$^+$ ELPs; right dot plots overlays show projection of CD19$^+$ cells (red dots) within the corresponding subsets; percentages are indicated.

(M and N) Immunophenotypic profiling of spleen CD19$^+$ or CD19$^-$ cellular subsets in humanized mice. Hu-CD45$^+$ cells isolated as above from the spleen of mice xenografted with neonatal or aged HSCs were analyzed as above; gates are set on the CD34$^-$ compartment followed by subdivision into CD19$^+$ or CD19$^-$ compartments. (M) Upper bar plot shows the subdivision of spleen CD19$^+$ BLs on the basis of forward scatter characteristic and differential CD20, IgM, or IgD expression; results are normalized relative to total CD19$^+$ cells. (N) Lower bar plot shows the relative percentages of the indicated CD56$^+$ NK, CD14$^+$ monocyte, CD141$^+$ cCD1, CD1c$^+$ cDC2, or CD117^{hi} mastocyte subsets; results are normalized relative to total CD19$^-$ cells. Circles correspond to individual mice; bars indicate medians; assessment of statistical significance is based on the unpaired t test (*p < 0.05 and ***p < 0.001).

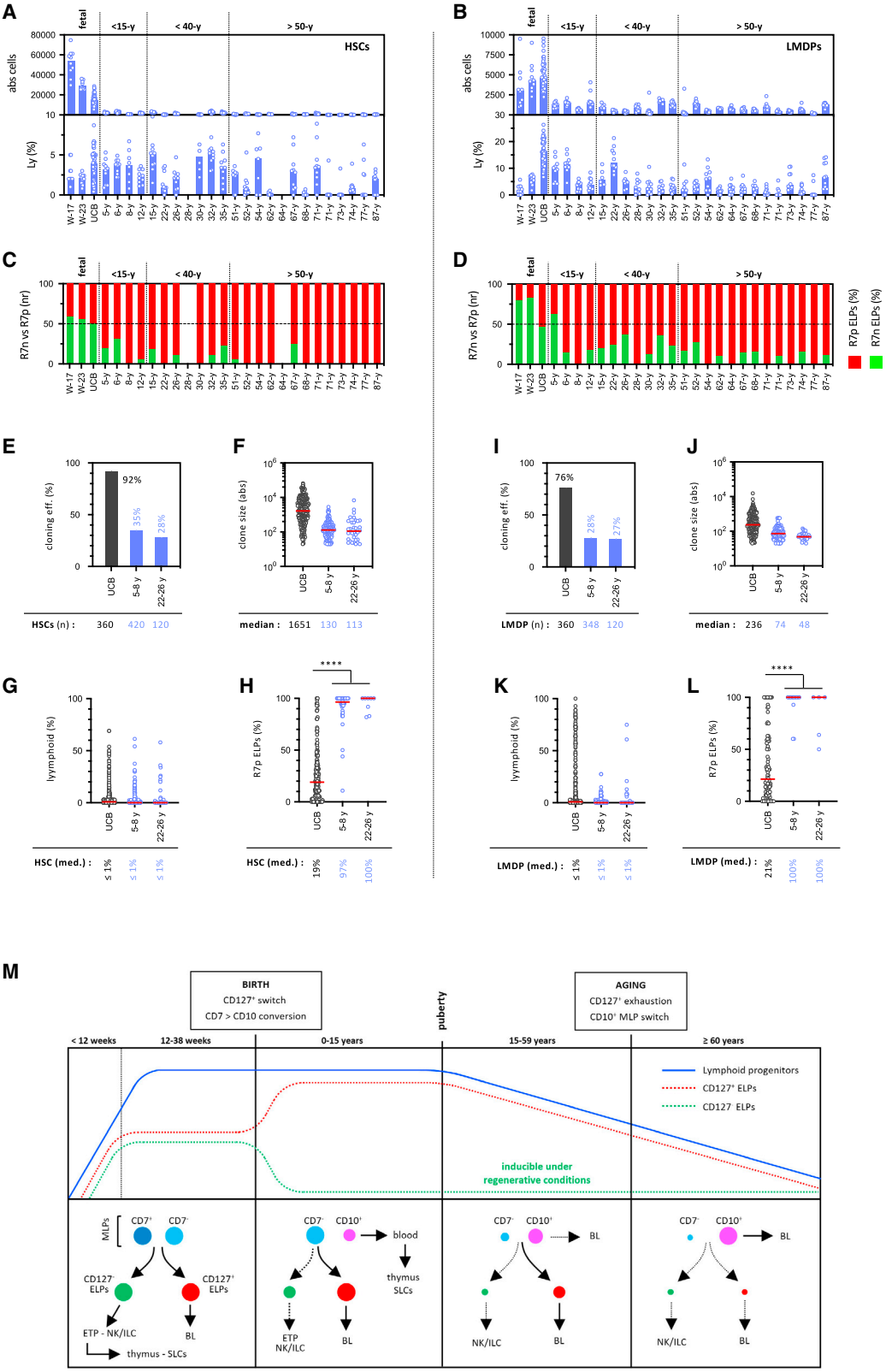

(legend on next page)

transplanted with aged HSCs, compared with ≥60% for those reconstituted with neonatal HSCs (Figure 6G). Also, consistent with the B-lineage bias of postnatal lymphopoiesis higher percentages of CD19$^+$ B lymphocytes were detected in mice transplanted with aged HSCs (Figure 6H). Spectral immunophenotyping of BM CD34^{hi} HSPCs confirmed that whereas the percentages of CD127$^+$ ELP percentages undergo a ≥3-fold decrease in mice reconstituted with aged HSC, those of CD10$^+$ MLPs increased by ≥35-fold and accounted for the majority of lymphoid progenitors (Figures 6I–6K). Further immunophenotyping confirmed that in mice transplanted with aged HSCs B cell differentiation undergoes a clear switch toward the CD10$^+$ MLP pathway (Figure 6L). Interestingly, detection of few CD7$^+$ ELPs in the BM of mice reconstituted with HSCs from older donors is concordant with clinical data showing *de novo* production of NK cells and ILCs in patients transplanted with adult HSCs.[33,34]

Analysis of mature cellular populations in the spleen found that the relative percentages of IgM$^-$ versus IgM$^+$ B lymphocytes vary in inverse proportions in mice reconstituted with neonatal or aged HSCs (Figure 6M). Finally, consistent with the established age-related myeloid bias in HSC differentiation potential,[35] analysis of mature cellular populations found that the percentage of spleen monocytes increases 4-fold in mice transplanted with aged HSCs, whereas those of NK cells, plasmacytoid DCs, or mastocytes decrease up to 10-fold (Figure 6N).

Collectively, these results indicate that similar to the fetal to postnatal transition lymphoid architecture and B cell differentiation pathways are subjected to a further developmental transition after the age of 60 years.

Ontogeny-related variations in lymphoid production patterns are developmentally programmed

To search for age-dependent variations in lymphoid potential, HSCs or LMDPs from 26 donors between 17 PCW and 87 years were subsequently seeded under *scf:tpo:tslp* condition (Figures 7A–7D). FACS analysis of their differentiated progeny confirmed that HSC expansion rates decrease rapidly after birth and showed that, conversely to myeloid granulocyte or monocyte production that remains stable over age (data not shown), lymphoid outputs follow a downward trend, especially in donors older than 50 years in whom high inter-individual and inter-clone differences are also observed. Similar age-dependent decline in lymphoid output is also seen in postnatal LMDPs after puberty which stresses the relevance of these findings. Most important, analyses of ELP production patterns confirmed that, in both HSC and LMDP compartments, transition to postnatal life is associated with a shift toward CD127$^+$ ELPs whose relative percentages also gradually increase over age. Overall similar proliferation and differentiation patterns were observed in cultures under *scf:g:gm* condition reinforcing the view that CD127$^+$ ELPs are subjected to a cell-intrinsic regulation (data not shown). Consistent with these results, single-cell differentiation assays showed that postnatal HSPCs have decreased cloning efficiency, reduced expansion rates, and display predominant CD127$^+$ ELP output (Figures 7E–7L). Immunophenotypic characterization of *in vitro* differentiated ELPs confirmed that CD7 expression decreases as a function of donor age but failed to disclose concomitant variation in the expression pattern of CD10 (Figure S7B), which argues for a more complex regulation of this marker. Last, culturing postnatal HSPCs under *scf:flt3l* condition revealed that, independent of the donor age, Flt3L fully restores the differentiation of the CD127$^-$ ELPs (Figure S7C).

Collectively, these results show that ontogeny-related changes in the patterns of lymphocyte production are developmentally imprinted at the level of HSCs. In addition, they suggest that preservation of Flt3L responsiveness in adult donors could help maintain lymphoid homeostasis throughout postnatal life.

DISCUSSION

In this study, we followed the variations in lymphoid development architecture and lymphocyte production patterns across development and aging. As well as resolving long-standing controversies as to the phenotype and function of MLPs, our data reveal that human lymphopoiesis undergoes three successive developmental transitions—the first at birth, then at puberty, and last during aging—indicating that the developmental complexity of the lymphoid lineage has to date been largely underestimated (Figure 7M; Table S6).

Figure 7. Ontogeny-related changes in lymphoid potential are orchestrated at the level of HSCs

(A–D) *In vitro* assessment of the lymphoid potential of fetal and postnatal CD34$^+$ HSPCs. The indicated HSC (left panels) or LMDP (right panels) fraction isolated from the UCB or BM of 26 donors between development week 17 and 87 years (Figure S6: gating strategy 3) were cultured for 10 days under the *scf:tslp:tpo* condition before quantification of lymphoid outputs. Bar plots show absolute cell numbers (upper panels) or percentages of lymphoid cells (lower panels) in (A) HSC or (B) LMDP cultures; bars indicate medians; circles correspond to individual wells. Stacked bar plots show the relative proportions of CD127$^-$ (green bars) and CD127$^+$ (red bars) ELPs in (C) HSC or (D) LMDP cultures; bars correspond to median percentages of ≥10 individual wells.

(E–L) Clonal diversification assays. HSCs (E–H) or LMDPs (I–L) isolated from the UCB or the BM of 4 postnatal donors between 5 and 8 years or 22 and 26 years. Cells were seeded individually in 96-well plates and cultured for 14 days onto OP9 stroma under the *scf:gm:tpo* before FACS analysis. Bar and circle plots respectively show (E and I) cloning efficiencies; (F and J) absolute cell numbers per clone; (G and K) total lymphoid cell percentage per clone; (H and L) percentages of CD127$^+$ ELPs per clone normalized relative to total ELPs; positivity threshold for ELP detection is set arbitrarily at ≥10 ELPs/clone. Red bars correspond to medians; corresponding values are indicated below each plot. Assessment of statistical significance was performed using the Mann-Whitney test (**$p < 0.01$, ***$p < 0.001$, and ****$p < 0.0001$).

(M) Model recapitulating the developmental transitions in lymphopoiesis occurring across ontogeny. Upper panels show the dynamics of lymphoid progenitors (plain blue line), as well as of CD127$^-$ (dashed green line) or CD127$^+$ ELPs (dashed red line). Lower panels show age-related changes in lymphoid differentiation pathways: plain and dashed arrows indicate predominant and accessory differentiation pathways; circle diameters correspond to the estimated size of the corresponding cell subsets. Dark blue circles, embryonic CD7$^+$ MLPs; light blue circles, fetal CD7$^-$ MLPs; purple circles, postnatal CD10$^+$ MLPs); green circles, CD127$^-$ ELPs; red circles, CD127$^+$ ELPs. SLCs, secondary lymphoid organs.

Subjecting neonatal progenitors to optimized sorting schemes found that CD127$^-$ and CD127$^+$ ELPs[17] circulate at low levels in UCB and confirmed that, among them, differential CD7 versus CD10 expression distinguishes NK/ILC/T from B lineage-polarized subsets.[14,28] As expected, these analyses also confirmed that CD127$^-$ and CD127$^+$ ELPs correspond to the immediate downstream progeny of lymphoid-restricted CD117^{lo} MLPs. Further investigation revealed that differential CD7 and CD10 expression allows distinction between embryonic, fetal, and postnatal MLPs and showed that, whereas embryonic CD7$^+$ MLPs display balanced ELP production patterns, their fetal CD7$^-$ and postnatal CD10$^+$ counterparts are increasingly biased toward CD127$^+$ ELPs and the subsequent generation of BLs. These results extend earlier reports that independent subsets of CD7$^+$[20,36] or CD10$^+$ MLPs[15,16] circulate in the neonatal blood. Transcriptional profiling confirmed the lymphoid status of neonatal MLPs but failed to disclose subset-specific gene signatures. As neonatal MLPs overexpressed *HES1-4* transcripts, our data also suggest that Notch signaling may contribute to lymphoid specification and/or to differential priming toward the CD127$^-$ or CD127$^+$ ELPs.

Dynamic follow-up of lymphoid progenitors in fetal and postnatal donors showed that lymphoid outputs remain at stable levels until puberty after which they undergo a gradual age-dependent decline.[37] Most important, these analyses also revealed that a developmental shift from fetal multilineage to postnatal B lineage-biased lymphopoiesis takes place within the first few days after birth. Transition to aerial life is associated with a global immunophenotypic CD7 to CD10 conversion of lymphoid progenitors and an increase in production of CD127$^+$ ELPs which persists until puberty. *In vitro* diversification assays then confirmed that these changes are developmentally imprinted and orchestrated at the level of HSCs. Thus, in addition to demonstrating the dual ontogeny and differentiation value of CD7 and CD10 markers, our results provide evidence that, in contrast to ELPs in which CD7 is indicative of specification toward the NK/ILC/T lineage,[14,17] the expression of CD7 by by more immature fetal or neonatal HSPCs reflects an early developmental origin. An embryonic origin of the CD7$^+$ HSCs is further supported by their gene signature consistent with a more primitive developmental status, which also suggests that these might correspond to human counterparts of recently described mouse embryonic multipotent progenitors (eMPPs).[10] Whether CD7 expression reflects a special susceptibility of embryonic HSPCs to Notch signaling and if its decreasing expression over age could represent a surrogate marker of the postnatal decline in T potential deserves further investigation.[38] On the other hand, the premature acquisition of CD10 by neonatal MLPs and ELPs can be considered as an immunophenotypic correlate of the B-lineage shift of postnatal lymphopoiesis.

Our results provide evidence that the biological function and differentiation status of CD10$^+$ MLPs change with age. Their robust enrichment in the blood of pediatric donors confirms that at least during the prepubertal period this population has a selective capacity to enter the blood flow and seed peripheral lymphoid organs, including thymus.[31,32] This issue is even more important that despite an intrinsic B lineage-bias CD10$^+$ MLPs are detected in the thymus of pediatric donors where they undergo a complex transcriptional rewiring to enter the T cell differentiation pathway.[39] Our observation that in pediatric donors CD127$^+$ ELPs differentiate independently of CD10$^+$ MLPs and upregulate CD10 and CD19 as they progress along the B-lymphoid pathway, strengthens the view that before puberty CD10$^+$ MLPs have only a marginal contribution to BM lymphopoiesis. Immunophenotypic profiling of lymphoid progenitors from adult donors added further complexity to this picture by demonstrating that with increasing age percentages of CD10$^+$ MLPs vary inversely with CD127$^+$ ELPs. In contrast to younger donors, in whom B cell differentiation proceeds via CD127$^+$ ELPs (whose highly proliferative status should also contribute to pre-commitment amplification of the B compartment), in donors over 60 years B cell differentiation starts directly at the level of the CD10$^+$ MLPs, bypassing CD127$^+$ ELPs. Analysis of immunodeficient mice reconstituted with aged HSCs confirmed that, in the same manner as the fetal to postnatal transition in lymphocyte production patterns, this late switch in the B cell differentiation pathways is developmentally imprinted at the level of HSCs.

Limitations of the study

Although the molecular bases of the neonatal shift in lymphocyte production patterns still need to be clarified, the temporal concordance with the fetal-to-adult switch in erythropoiesis strongly argues for involvement of conserved gene regulatory networks.[40] Consistent with this view, Lin28b, ZBTB7A and BCL11A which control hemoglobin switching[41,42] are key regulators of lymphopoiesis.[43–45] Mechanisms underlying the late transition in B cell differentiation pathways deserve further investigation.

Despite these limitations, this study may contribute to a better understanding of the dynamics of lymphocyte production patterns during development and aging. Our results indicate that whereas fetal lymphopoiesis allows prenatal acquisition of diversified T and B cell repertoires essential to reach immunocompetence at birth, the neonatal boost in B cell production may be important to help broaden the antibody repertoire and enhance antibody-mediated immune responses to reduce morbidity and mortality due to infections during infancy. Whether the shift in lymphopoiesis taking place after birth contributes to the postnatal decline in T cell production[46] and or to age-related differences in the incidence of B and T cell acute lymphoblastic leukemia[47] should be the subject of future studies.

STAR★METHODS

Detailed methods are provided in the online version of this paper and include the following:

- KEY RESOURCES TABLE
- RESOURCE AVAILABILITY
  - Lead contact
  - Materials availability
  - Data and code availability
- EXPERIMENTAL MODEL AND SUBJECT DETAILS
  - Human sample collection
  - Mice

- METHOD DETAILS
  - Processing of human tissues and cell separation
  - Xeno-transplantations
  - Flow cytometry and cell sorting
  - Spectral cytometry
  - Cell cultures and analysis
- QUANTIFICATION AND STATISTICAL ANALYSIS
  - Algorithm-assisted clone classification
  - ATAC-seq analysis and bioinformatics
  - Mini-RNA-seq analysis and bioinformatics

SUPPLEMENTAL INFORMATION

Supplemental information can be found online at https://doi.org/10.1016/j.celrep.2023.112618.

ACKNOWLEDGMENTS

The authors thank Christelle Doliger, Niclas Setterblad, and Claire Maillard (Plateforme d'Imagerie et de Tri Cellulaire, IRSL, Paris, France). We are grateful to Laurent David (Inserm 1064, Nantes, France) and Bernard Jost (GenomEast platform, IGBMC, Strasbourg, France). We also thank Jean Christophe Bories and Michele Souyri for critical discussions. This work was supported by the Agence de la Biomédecine, Agence National de la Recherche (ANR EpiDev), the Institut National Du Cancer (InCA B-REC), the Fondation Ramsay Générale de Santé, and by the INSERM HuDeCA network.

AUTHOR CONTRIBUTIONS

S.K., E.C., S.L., and Z.K. designed and performed most experiments; S. Diop and F.J. analyzed the clonal data; S. Duchez and E.N. conducted the mouse studies; J.L. and T. Domet provided the UCB; M.S., C.A., and F.G. provided the fetal and adult BM samples; A.C., E.V., and E.AM. contributed to data analyses and wrote the paper; D.G. and M.G. performed the ATAC-seq analyses; F.C., B.E., and T. Darde performed the transcriptome analyses; K.A.H. and B.C. ensured the scientific supervision of the project and wrote the paper. All authors read and approved the manuscript.

DECLARATION OF INTERESTS

The authors declare no competing interests.

Received: February 16, 2023
Revised: April 13, 2023
Accepted: May 22, 2023

REFERENCES

1. Hayakawa, K., Hardy, R.R., Herzenberg, L.A., and Herzenberg, L.A. (1985). Progenitors for Ly-1 B cells are distinct from progenitors for other B cells. J. Exp. Med. *161*, 1554–1568. https://doi.org/10.1084/jem.161.6.1554.
2. Herzenberg, L.A., and Herzenberg, L.A. (1989). Toward a layered immune system. Cell *59*, 953–954.
3. Montecino-Rodriguez, E., Fice, M., Casero, D., Berent-Maoz, B., Barber, C.L., and Dorshkind, K. (2016). Distinct genetic networks orchestrate the emergence of specific waves of fetal and adult B-1 and B-2 development. Immunity *45*, 527–539. https://doi.org/10.1016/j.immuni.2016.07.012.
4. Elsaid, R., Meunier, S., Burlen-Defranoux, O., Soares-da-Silva, F., Perchet, T., Iturri, L., Freyer, L., Vieira, P., Pereira, P., Golub, R., et al. (2021). A wave of bipotent T/ILC-restricted progenitors shapes the embryonic thymus microenvironment in a time-dependent manner. Blood *137*, 1024–1036. https://doi.org/10.1182/blood.2020006779.
5. Adolfsson, J., Månsson, R., Buza-Vidas, N., Hultquist, A., Liuba, K., Jensen, C.T., Bryder, D., Yang, L., Borge, O.J., Thoren, L.A.M., et al. (2005). Identification of Flt3+ lympho-myeloid stem cells lacking erythro-megakaryocytic potential a revised road map for adult blood lineage commitment. Cell *121*, 295–306. https://doi.org/10.1016/j.cell.2005.02.013.
6. Cabezas-Wallscheid, N., Klimmeck, D., Hansson, J., Lipka, D.B., Reyes, A., Wang, Q., Weichenhan, D., Lier, A., von Paleske, L., Renders, S., et al. (2014). Identification of regulatory networks in HSCs and their immediate progeny via integrated proteome, transcriptome, and DNA methylome analysis. Cell Stem Cell *15*, 507–522. https://doi.org/10.1016/j.stem.2014.07.005.
7. Amann-Zalcenstein, D., Tian, L., Schreuder, J., Tomei, S., Lin, D.S., Fairfax, K.A., Bolden, J.E., McKenzie, M.D., Jarratt, A., Hilton, A., et al. (2020). A new lymphoid-primed progenitor marked by Dach1 downregulation identified with single cell multi-omics. Nat. Immunol. *21*, 1574–1584. https://doi.org/10.1038/s41590-020-0799-x.
8. Berthault, C., Ramond, C., Burlen-Defranoux, O., Soubigou, G., Chea, S., Golub, R., Pereira, P., Vieira, P., and Cumano, A. (2017). Asynchronous lineage priming determines commitment to T cell and B cell lineages in fetal liver. Nat. Immunol. *18*, 1139–1149. https://doi.org/10.1038/ni.3820.
9. Kawamoto, H., Ikawa, T., Ohmura, K., Fujimoto, S., and Katsura, Y. (2000). T cell progenitors emerge earlier than B cell progenitors in the murine fetal liver. Immunity *12*, 441–450. https://doi.org/10.1016/s1074-7613(00)80196-x.
10. Patel, S.H., Christodoulou, C., Weinreb, C., Yu, Q., da Rocha, E.L., Pepe-Mooney, B.J., Bowling, S., Li, L., Osorio, F.G., Daley, G.Q., and Camargo, F.D. (2022). Lifelong multilineage contribution by embryonic-born blood progenitors. Nature *606*, 747–753. https://doi.org/10.1038/s41586-022-04804-z.
11. Yokomizo, T., Ideue, T., Morino-Koga, S., Tham, C.Y., Sato, T., Takeda, N., Kubota, Y., Kurokawa, M., Komatsu, N., Ogawa, M., et al. (2022). Independent origins of fetal liver haematopoietic stem and progenitor cells. Nature *609*, 779–784. https://doi.org/10.1038/s41586-022-05203-0.
12. Doulatov, S., Notta, F., Laurenti, E., and Dick, J.E. (2012). Hematopoiesis: a human perspective. Cell Stem Cell *10*, 120–136. https://doi.org/10.1016/j.stem.2012.01.006.
13. Galy, A., Travis, M., Cen, D., and Chen, B. (1995). Human T, B, natural killer, and dendritic cells arise from a common bone marrow progenitor cell subset. Immunity *3*, 459–473.
14. Haddad, R., Guardiola, P., Izac, B., Thibault, C., Radich, J., Delezoide, A.L., Baillou, C., Lemoine, F.M., Gluckman, J.C., Pflumio, F., and Canque, B. (2004). Molecular characterization of early human T/NK and B-lymphoid progenitor cells in umbilical cord blood. Blood *104*, 3918–3926. https://doi.org/10.1182/blood-2004-05-1845 2004-05-1845.
15. Doulatov, S., Notta, F., Eppert, K., Nguyen, L.T., Ohashi, P.S., and Dick, J.E. (2010). Revised map of the human progenitor hierarchy shows the origin of macrophages and dendritic cells in early lymphoid development. Nat. Immunol. *11*, 585–593. https://doi.org/10.1038/ni.1889.
16. Karamitros, D., Stoilova, B., Aboukhalil, Z., Hamey, F., Reinisch, A., Samitsch, M., Quek, L., Otto, G., Repapi, E., Doondeea, J., et al. (2018). Single-cell analysis reveals the continuum of human lympho-myeloid progenitor cells. Nat. Immunol. *19*, 85–97. https://doi.org/10.1038/s41590-017-0001-2.
17. Alhaj Hussen, K., Vu Manh, T.P., Guimiot, F., Nelson, E., Chabaane, E., Delord, M., Barbier, M., Berthault, C., Dulphy, N., Alberdi, A.J., et al. (2017). Molecular and functional characterization of lymphoid progenitor subsets reveals a bipartite architecture of human lymphopoiesis. Immunity *47*, 680–696.e8. https://doi.org/10.1016/j.immuni.2017.09.009.
18. O'Byrne, S., Elliott, N., Rice, S., Buck, G., Fordham, N., Garnett, C., Godfrey, L., Crump, N.T., Wright, G., Inglott, S., et al. (2019). Discovery of a CD10-negative B-progenitor in human fetal life identifies unique ontogeny-related developmental programs. Blood *134*, 1059–1071. https://doi.org/10.1182/blood.2019001289.

19. Hao, Q.L., Zhu, J., Price, M.A., Payne, K.J., Barsky, L.W., and Crooks, G.M. (2001). Identification of a novel, human multilymphoid progenitor in cord blood. Blood *97*, 3683–3690.

20. Hoebeke, I., De Smedt, M., Stolz, F., Pike-Overzet, K., Staal, F.J.T., Plum, J., and Leclercq, G. (2007). T-B- and NK-lymphoid, but not myeloid cells arise from human CD34(+)CD38(-)CD7(+) common lymphoid progenitors expressing lymphoid-specific genes. Leukemia *21*, 311–319. https://doi.org/10.1038/sj.leu.2404488.

21. Martin, E.W., Krietsch, J., Reggiardo, R.E., Sousae, R., Kim, D.H., and Forsberg, E.C. (2021). Chromatin accessibility maps provide evidence of multilineage gene priming in hematopoietic stem cells. Epigenet. Chromatin *14*, 2. https://doi.org/10.1186/s13072-020-00377-1.

22. Lara-Astiaso, D., Weiner, A., Lorenzo-Vivas, E., Zaretsky, I., Jaitin, D.A., David, E., Keren-Shaul, H., Mildner, A., Winter, D., Jung, S., et al. (2014). Immunogenetics. Chromatin state dynamics during blood formation. Science *345*, 943–949. https://doi.org/10.1126/science.1256271.

23. Laurenti, E., Doulatov, S., Zandi, S., Plumb, I., Chen, J., April, C., Fan, J.B., and Dick, J.E. (2013). The transcriptional architecture of early human hematopoiesis identifies multilevel control of lymphoid commitment. Nat. Immunol. *14*, 756–763. https://doi.org/10.1038/ni.2615.

24. Stehling-Sun, S., Dade, J., Nutt, S.L., DeKoter, R.P., and Camargo, F.D. (2009). Regulation of lymphoid versus myeloid fate 'choice' by the transcription factor Mef2c. Nat. Immunol. *10*, 289–296. https://doi.org/10.1038/ni.1694.

25. Hulea, L., and Nepveu, A. (2012). CUX1 transcription factors: from biochemical activities and cell-based assays to mouse models and human diseases. Gene *497*, 18–26. https://doi.org/10.1016/j.gene.2012.01.039.

26. García-Prat, L., Kaufmann, K.B., Schneiter, F., Voisin, V., Murison, A., Chen, J., Chan-Seng-Yue, M., Gan, O.I., McLeod, J.L., Smith, S.A., et al. (2021). TFEB-mediated endolysosomal activity controls human hematopoietic stem cell fate. Cell Stem Cell *28*, 1838–1850. https://doi.org/10.1016/j.stem.2021.07.003.

27. Huot, G., Vernier, M., Bourdeau, V., Doucet, L., Saint-Germain, E., Gaumont-Leclerc, M.F., Moro, A., and Ferbeyre, G. (2014). CHES1/FOXN3 regulates cell proliferation by repressing PIM2 and protein biosynthesis. Mol. Biol. Cell *25*, 554–565. https://doi.org/10.1091/mbc.E13-02-0110.

28. Haddad, R., Guimiot, F., Six, E., Jourquin, F., Setterblad, N., Kahn, E., Yagello, M., Schiffer, C., Andre-Schmutz, I., Cavazzana-Calvo, M., et al. (2006). Dynamics of thymus-colonizing cells during human development. Immunity *24*, 217–230. https://doi.org/10.1016/j.immuni.2006.01.008.

29. Roy, A., Wang, G., Iskander, D., O'Byrne, S., Elliott, N., O'Sullivan, J., Buck, G., Heuston, E.F., Wen, W.X., Meira, A.R., et al. (2021). Transitions in lineage specification and gene regulatory networks in hematopoietic stem/progenitor cells over human development. Cell Rep. *36*, 109698. https://doi.org/10.1016/j.celrep.2021.109698.

30. Satoh, Y., Yokota, T., Sudo, T., Kondo, M., Lai, A., Kincade, P.W., Kouro, T., Iida, R., Kokame, K., Miyata, T., et al. (2013). The Satb1 protein directs hematopoietic stem cell differentiation toward lymphoid lineages. Immunity *38*, 1105–1115. https://doi.org/10.1016/j.immuni.2013.05.014.

31. Lavaert, M., Liang, K.L., Vandamme, N., Park, J.E., Roels, J., Kowalczyk, M.S., Li, B., Ashenberg, O., Tabaka, M., Dionne, D., et al. (2020). Integrated scRNA-seq identifies human postnatal thymus seeding progenitors and regulatory dynamics of differentiating immature thymocytes. Immunity *52*, 1088–1104. https://doi.org/10.1016/j.immuni.2020.03.019.

32. Six, E.M., Bonhomme, D., Monteiro, M., Beldjord, K., Jurkowska, M., Cordier-Garcia, C., Garrigue, A., Dal Cortivo, L., Rocha, B., Fischer, A., et al. (2007). A human postnatal lymphoid progenitor capable of circulating and seeding the thymus. J. Exp. Med. *204*, 3085–3093. https://doi.org/10.1084/jem.20071003.

33. Park, B.G., Park, C.J., Jang, S., Chi, H.S., Kim, D.Y., Lee, J.H., Lee, J.H., and Lee, K.H. (2015). Reconstitution of lymphocyte subpopulations after hematopoietic stem cell transplantation: comparison of hematologic malignancies and donor types in event-free patients. Leuk. Res. *39*, 1334–1341. https://doi.org/10.1016/j.leukres.2015.09.010.

34. Russo, A., Oliveira, G., Berglund, S., Greco, R., Gambacorta, V., Cieri, N., Toffalori, C., Zito, L., Lorentino, F., Piemontese, S., et al. (2018). NK cell recovery after haploidentical HSCT with posttransplant cyclophosphamide: dynamics and clinical implications. Blood *131*, 247–262. https://doi.org/10.1182/blood-2017-05-780668.

35. Kuranda, K., Vargaftig, J., de la Rochere, P., Dosquet, C., Charron, D., Bardin, F., Tonnelle, C., Bonnet, D., and Goodhardt, M. (2011). Age-related changes in human hematopoietic stem/progenitor cells. Aging Cell *10*, 542–546. https://doi.org/10.1111/j.1474-9726.2011.00675.x.

36. Hao, Q.L., George, A.A., Zhu, J., Barsky, L., Zielinska, E., Wang, X., Price, M., Ge, S., and Crooks, G.M. (2008). Human intrathymic lineage commitment is marked by differential CD7 expression: identification of CD7- lympho-myeloid thymic progenitors. Blood *111*, 1318–1326. https://doi.org/10.1182/blood-2007-08-106294.

37. Rossi, M.I.D., Yokota, T., Medina, K.L., Garrett, K.P., Comp, P.C., Schipul, A.H., Jr., and Kincade, P.W. (2003). B lymphopoiesis is active throughout human life, but there are developmental age-related changes. Blood *101*, 576–584. https://doi.org/10.1182/blood-2002-03-0896.

38. Haynes, B.F., Markert, M.L., Sempowski, G.D., Patel, D.D., and Hale, L.P. (2000). The role of the thymus in immune reconstitution in aging, bone marrow transplantation, and HIV-1 infection. Annu. Rev. Immunol. *18*, 529–560. https://doi.org/10.1146/annurev.immunol.18.1.529.

39. Cordes, M., Canté-Barrett, K., van den Akker, E.B., Moretti, F.A., Kiełbasa, S.M., Vloemans, S.A., Garcia-Perez, L., Teodosio, C., van Dongen, J.J.M., Pike-Overzet, K., et al. (2022). Single-cell immune profiling reveals thymus-seeding populations, T cell commitment, and multilineage development in the human thymus. Sci. Immunol. *7*, eade0182. https://doi.org/10.1126/sciimmunol.ade0182.

40. Sankaran, V.G., and Orkin, S.H. (2013). The switch from fetal to adult hemoglobin. Cold Spring Harb. Perspect. Med. *3*, a011643. https://doi.org/10.1101/cshperspect.a011643.

41. Basak, A., Munschauer, M., Lareau, C.A., Montbleau, K.E., Ulirsch, J.C., Hartigan, C.R., Schenone, M., Lian, J., Wang, Y., Huang, Y., et al. (2020). Control of human hemoglobin switching by LIN28B-mediated regulation of BCL11A translation. Nat. Genet. *52*, 138–145. https://doi.org/10.1038/s41588-019-0568-7.

42. Masuda, T., Wang, X., Maeda, M., Canver, M.C., Sher, F., Funnell, A.P.W., Fisher, C., Suciu, M., Martyn, G.E., Norton, L.J., et al. (2016). Transcription factors LRF and BCL11A independently repress expression of fetal hemoglobin. Science *351*, 285–289. https://doi.org/10.1126/science.aad3312.

43. Maeda, T., Merghoub, T., Hobbs, R.M., Dong, L., Maeda, M., Zakrzewski, J., van den Brink, M.R.M., Zelent, A., Shigematsu, H., Akashi, K., et al. (2007). Regulation of B versus T lymphoid lineage fate decision by the proto-oncogene LRF. Science *316*, 860–866. https://doi.org/10.1126/science.1140881.

44. Yu, Y., Wang, J., Khaled, W., Burke, S., Li, P., Chen, X., Yang, W., Jenkins, N.A., Copeland, N.G., Zhang, S., and Liu, P. (2012). Bcl11a is essential for lymphoid development and negatively regulates p53. J. Exp. Med. *209*, 2467–2483. https://doi.org/10.1084/jem.20121846.

45. Yuan, J., Nguyen, C.K., Liu, X., Kanellopoulou, C., and Muljo, S.A. (2012). Lin28b reprograms adult bone marrow hematopoietic progenitors to mediate fetal-like lymphopoiesis. Science *335*, 1195–1200. https://doi.org/10.1126/science.1216557.

46. Haynes, B.F., Sempowski, G.D., Wells, A.F., and Hale, L.P. (2000). The human thymus during aging. Immunol. Res. *22*, 253–261. https://doi.org/10.1385/IR:22:2-3:253.

47. Swaminathan, S., Klemm, L., Park, E., Papaemmanuil, E., Ford, A., Kweon, S.M., Trageser, D., Hasselfeld, B., Henke, N., Mooster, J., et al. (2015). Mechanisms of clonal evolution in childhood acute lymphoblastic leukemia. Nat. Immunol. *16*, 766–774. https://doi.org/10.1038/ni.3160.

48. Corces, M.R., Trevino, A.E., Hamilton, E.G., Greenside, P.G., Sinnott-Armstrong, N.A., Vesuna, S., Satpathy, A.T., Rubin, A.J., Montine, K.S., Wu, B., et al. (2017). An improved ATAC-seq protocol reduces background and

enables interrogation of frozen tissues. Nat. Methods *14*, 959–962. https://doi.org/10.1038/nmeth.4396.

49. Buenrostro, J.D., Wu, B., Chang, H.Y., and Greenleaf, W.J. (2015). ATAC-seq: a method for assaying chromatin accessibility genome-wide. Curr. Protoc. Mol. Biol. *109*, 21.29.1–21.29.9. https://doi.org/10.1002/0471142727.mb2129s109.
50. Cacchiarelli, D., Trapnell, C., Ziller, M.J., Soumillon, M., Cesana, M., Karnik, R., Donaghey, J., Smith, Z.D., Ratanasirintrawoot, S., Zhang, X., et al. (2015). Integrative analyses of human reprogramming reveal dynamic nature of induced pluripotency. Cell *162*, 412–424. https://doi.org/10.1016/j.cell.2015.06.016.
51. Becht, E., McInnes, L., Healy, J., Dutertre, C.A., Kwok, I.W.H., Ng, L.G., Ginhoux, F., and Newell, E.W. (2018). Dimensionality reduction for visualizing single-cell data using UMAP. Nat. Biotechnol. *37*, 38–44. https://doi.org/10.1038/nbt.4314.
52. Pedregosa, F., Varoquaux, G., Gramfort, A., Michel, V., Thirion, B., Grisel, O., Blondel, M., Prettenhofer, P., Weiss, R., Dubourg, V., et al. (2011). Scikit-learn: machine learning in Python. J. Mach. Learn. Res. *12*, 2825–2830.
53. Quinlan, A.R., and Hall, I.M. (2010). BEDTools: a flexible suite of utilities for comparing genomic features. Bioinformatics *26*, 841–842. https://doi.org/10.1093/bioinformatics/btq033.
54. Liao, Y., Smyth, G.K., and Shi, W. (2014). featureCounts: an efficient general purpose program for assigning sequence reads to genomic features. Bioinformatics *30*, 923–930. https://doi.org/10.1093/bioinformatics/btt656.
55. Robinson, M.D., McCarthy, D.J., and Smyth, G.K. (2010). edgeR: a Bioconductor package for differential expression analysis of digital gene expression data. Bioinformatics *26*, 139–140. https://doi.org/10.1093/bioinformatics/btp616.
56. Ramírez, F., Ryan, D.P., Grüning, B., Bhardwaj, V., Kilpert, F., Richter, A.S., Heyne, S., Dündar, F., and Manke, T. (2016). deepTools2: a next generation web server for deep-sequencing data analysis. Nucleic Acids Res. *44*, W160–W165. https://doi.org/10.1093/nar/gkw257.
57. Yu, G., Wang, L.G., and He, Q.Y. (2015). ChIPseeker: an R/Bioconductor package for ChIP peak annotation, comparison and visualization. Bioinformatics *31*, 2382–2383. https://doi.org/10.1093/bioinformatics/btv145.
58. McLean, C.Y., Bristor, D., Hiller, M., Clarke, S.L., Schaar, B.T., Lowe, C.B., Wenger, A.M., and Bejerano, G. (2010). GREAT improves functional interpretation of cis-regulatory regions. Nat. Biotechnol. *28*, 495–501. https://doi.org/10.1038/nbt.1630.
59. Bailey, T.L., Johnson, J., Grant, C.E., and Noble, W.S. (2015). The MEME suite. Nucleic Acids Res. *43*, W39–W49. https://doi.org/10.1093/nar/gkv416.
60. Giacosa, S., Pillet, C., Séraudie, I., Guyon, L., Wallez, Y., Roelants, C., Battail, C., Evrard, B., Chalmel, F., Barette, C., et al. (2021). Cooperative blockade of CK2 and ATM kinases drives apoptosis in VHL-deficient renal carcinoma cells through ROS overproduction. Cancers *13*, 576. https://doi.org/10.3390/cancers13030576.
61. Love, M.I., Huber, W., and Anders, S. (2014). Moderated estimation of fold change and dispersion for RNA-seq data with DESeq2. Genome Biol. *15*, 550. https://doi.org/10.1186/s13059-014-0550-8.
62. Chalmel, F., and Primig, M. (2008). The Annotation, Mapping, Expression and Network (AMEN) suite of tools for molecular systems biology. BMC Bioinf. *9*, 86. https://doi.org/10.1186/1471-2105-9-86.
63. Ritchie, J.B., Tovar, D.A., and Carlson, T.A. (2015). Emerging object representations in the visual system predict reaction times for categorization. PLoS Comput. Biol. *11*, e1004316. https://doi.org/10.1371/journal.pcbi.1004316.
64. Smyth, G.K. (2004). Linear models and empirical bayes methods for assessing differential expression in microarray experiments. Stat. Appl. Genet. Mol. Biol. *3*, Article3. https://doi.org/10.2202/1544-6115.1027.
65. Subramanian, A., Tamayo, P., Mootha, V.K., Mukherjee, S., Ebert, B.L., Gillette, M.A., Paulovich, A., Pomeroy, S.L., Golub, T.R., Lander, E.S., and Mesirov, J.P. (2005). Gene set enrichment analysis: a knowledge-based approach for interpreting genome-wide expression profiles. Proc. Natl. Acad. Sci. USA *102*, 15545–15550. https://doi.org/10.1073/pnas.0506580102.
66. Kolmykov, S., Yevshin, I., Kulyashov, M., Sharipov, R., Kondrakhin, Y., Makeev, V.J., Kulakovskiy, I.V., Kel, A., and Kolpakov, F. (2021). GTRD: an integrated view of transcription regulation. Nucleic Acids Res. *49*, D104–D111. https://doi.org/10.1093/nar/gkaa1057.
67. Xie, X., Lu, J., Kulbokas, E.J., Golub, T.R., Mootha, V., Lindblad-Toh, K., Lander, E.S., and Kellis, M. (2005). Systematic discovery of regulatory motifs in human promoters and 3' UTRs by comparison of several mammals. Nature *434*, 338–345. https://doi.org/10.1038/nature03441.

STAR★METHODS

KEY RESOURCES TABLE

REAGENT or RESOURCE	SOURCE	IDENTIFIER
Antibodies		
anti-human CD45 AF700	BioLegend	Cat# 304024; RRID:AB_493761
anti-human CD34 Pacific Blue	BioLegend	Cat# 343512; RRID:AB_1877197
anti-human CD7 FITC	Beckman Coulter	Cat# A07755
anti-human CD38 PerCPCy5.5	BioLegend	Cat# 303522; RRID:AB_893314
anti-human CD33 BV785	BioLegend	Cat# 303427; RRID:AB_2650887
anti-human CD115 APC	BioLegend	Cat# 347306; RRID:AB_2562441
anti-human CD71 PE	BD Biosciences	Cat# 555537; RRID:AB_395921
anti-human ITGB7 PECy7	ThermoFisher	Cat# 25-5867-42; RRID:AB_2573481
anti-human CD3 PE-CF594	BD Biosciences	Cat# 562310; RRID:AB_11153505
anti-human CD14 PE-CF594	BD Biosciences	Cat# 562335; RRID:AB_11153663
anti-human CD19 PE-DAZZLE	BioLegend	Cat# 302252; RRID:AB_2563560
anti-human CD24 PE-CF594	BD Biosciences	Cat# 562405; RRID:AB_11153321
anti-human CD56 PE-CF594	BD Biosciences	Cat# 562289; RRID:AB_11152080
anti-human CD45RA BV711	BioLegend	Cat# 304138; RRID:AB_2563815
anti-human CD116 APC-vio770	Miltenyi	Cat# 130-100-992; RRID:AB_2654571
anti-human CD127 PECy5	BioLegend	Cat# 351324; RRID:AB_10915554
anti-human CD117 BV605	BioLegend	Cat# 313218; RRID:AB_2562025
anti-human CD10 BV650	BD Biosciences	Cat# 563734; RRID:AB_2738393
anti-human CD123 PE-Cy5.5	Beckman Coulter	Cat# B20022
anti-human CD45RA PE	BD Biosciences	Cat# 555489; RRID:AB_395880
anti-human CD19 BV711	BD Biosciences	Cat# 302245; RRID:AB_2562062
anti-human CD45 PerCp	BioLegend	Cat# 304025; RRID:AB_893341
anti-human CD34 BUV615	BD Biosciences	Cat# 751630; RRID:AB_2875623
anti-human CD45RA BUV395	BD Biosciences	Cat# 563791
anti-human CD38 APC-Fire 810	BioLegend	Cat# 303549; RRID:AB_2860783
anti-human CD33 PE-DAZZLE	BioLegend	Cat# 303431: RRID:AB_2734262
anti-human CD71 PECy5	BD Biosciences	Cat# 551143; RRID:AB_394071
anti-human CD123 SB436	ThermoFisher	Cat# 62-1239-42; RRID:AB_2662727
anti-human CD127 APC-R700	BD Biosciences	Cat# 565185; RRID:AB_2739099
anti-human CD2 PerCPCy5.5	BioLegend	Cat# 300216; RRID:AB_2561923
anti-human CD19 Spark NIR 685	BioLegend	Cat# 302269; RRID:AB_2860769
anti-human CD24 PE-AF 610	ThermoFisher	Cat# MHCD2422; RRID:AB_10375871
anti-human CD20 Pacific Orange	ThermoFisher	Cat# MHCD2030; RRID:AB_10375578
anti-human IgM BV570	BioLegend	Cat# 314517; RRID:AB_10913816
anti-human IgD BV480	BD Biosciences	Cat# 566187; RRID:AB_2739583
anti-human CD5 BV785	BD Biosciences	Cat# 740963; RRID:AB_2740588
anti-human CD56 BUV737	BD Biosciences	Cat# 612767; RRID:AB_2860005
anti-human CD94 PE	BD Biosciences	Cat# 555889; RRID:AB_396201
anti-human CD3 BUV661	BD Biosciences	Cat# 612965; RRID:AB_2916886
anti-human CD1c AF647	BD Biosciences	Cat# 565049
anti-human CD141 BB515	BD Biosciences	Cat# 566017; RRID:AB_2739462
anti-human CD303 BV750	BD Biosciences	Cat# 748001; RRID:AB_2872462
anti-human CD304 BV711	BioLegend	Cat# 354533; RRID:AB_2876674

(*Continued on next page*)

Continued

REAGENT or RESOURCE	SOURCE	IDENTIFIER
anti-human CD14 Spark Blue 550	BioLegend	Cat# 367147; RRID:AB_2820021
anti-human CD16 BUV496	BD Biosciences	Cat# 612945
anti-human CD15 BUV805	BD Biosciences	Cat# 742057; RRID:AB_2871345
anti-human CD7 BV510	BD Biosciences	Cat# 563650; RRID:AB_2713913
anti-human CD5 APC	BD Biosciences	Cat# 555355; RRID:AB_398594
anti-human CD4 FITC	BioLegend	Cat# 300506; RRID:AB_314074
anti-human CD8a PECy7	BioLegend	Cat# 301012; RRID:AB_314130
anti-human CD56 PECy7	BioLegend	Cat# 304628; RRID:AB_2149542
anti-human CD94 APC	BioLegend	Cat# 305508; RRID:AB_2133129
anti-human CD19 APC	BioLegend	Cat# 302212; RRID:AB_314242
anti-human CD9 PE-CF594	BD Biosciences	Cat# 563641; RRID:AB_2738340
anti-human CD20 APC	BioLegend	Cat# 302309; RRID:AB_314257
anti-human CD24 BV786	BD Biosciences	Cat# 740971; RRID:AB_2740596
anti-human CD123 BV786	BD Biosciences	Cat# 564196; RRID:AB_2738662
anti-human CD15 BV605	BD Biosciences	Cat# 562979; RRID:AB_2744292
Zombie UV	BioLegend	Cat# 423107
Biological samples		
Postnatal bone marrow	Unité de Thérapie Cellulaire, Saint-Louis Hospital (Paris)	N/A
Fetal and Postnatal Blood	Service de Biologie du Développement, Robert Debré Hospital (Paris)	N/A
Fetal bone marrow Fetal Liver	Service de Biologie du Développement, Robert Debré Hospital (Paris)	N/A
Umbilical cord blood	Unité de Thérapie Cellulaire of Hôpital Saint-Louis (Paris)	N/A
Chemicals, peptides, and recombinant proteins		
BIT 9500	StemCell Technologies	Cat#09500
Bovine serum albumin	Eurobio	Cat#GAUBSA0165
Dimethyl sulfoxide	Sigma Aldrich	Cat#D4540
Fc receptor-binding inhibitor	eBioscience	Cat#16-9161-73
Fetal calf serum	Life Technologies	Cat#10270106
Ficoll-Hypaque	Pancoll, PAN Biotech GmbH	Cat#P04-60500
Human FLT3L, premium grade	Miltenyi Biotech	Cat#130-096-479
Human G-CSF, premium grade	Miltenyi Biotech	Cat#130-093-861
Human TSLP, research grade	Miltenyi Biotech	Cat#130-106-270
Human GM-CSF, premium grade	Miltenyi Biotech	Cat#130-093-866
Human IL-2 IS, premium grade	Miltenyi Biotech	Cat#130-097-744
Human IL-3, premium grade	Miltenyi Biotech	Cat#130-095-069
Human IL-7, premium grade	Miltenyi Biotech	Cat#130-095-363
Human IL-15, premium grade	Miltenyi Biotech	Cat#130-095-765
Human M-CSF, premium grade	Miltenyi Biotech	Cat#130-096-492
Human SCF, premium grade	Miltenyi Biotech	Cat#130-096-695
Human TPO, premium grade	Miltenyi Biotech	Cat#130-095-752
RNase-free DNase I	Roche	Cat#1284932
SUPERase-In RNase Inhibitor	Ambion	Cat#AM2694
2-mercaptoethanol	Life Technologies	Cat#31350010
Maxima H Minus Reverse Transcriptase	Thermo Fisher	Cat# EP0752
Exonuclease	New EnglandBiolabs	Cat# M0293L

(*Continued on next page*)

Continued

REAGENT or RESOURCE	SOURCE	IDENTIFIER
Critical commercial assays		
CD34 Microbead kit	Miltenyi Biotech	Cat#130-046-702
Mouse Cell Depletion Kit	Miltenyi Biotech	Cat#130-104-694
DNA Clean and Concentrtor TM-5	ZYMO RESEARCH	Cat#D4013
Advantage 2 PCR Kit	Clontech	Cat#639206
Agencourt AMPure XP	Beckman Coulter	Cat#A63880
Nextera DNA Flex Library Prep	Illumina	Cat# 20018704
Deposited data		
Raw and pre-processed data	This paper	GSE215045
Raw and pre-processed data	This paper	GSE215052
Experimental models: Cell lines		
Mouse: OP9	A. Cumano, Institut Pasteur	N/A
Mouse: OP9-DL4	A. Cumano, Institut Pasteur	N/A
Mouse: MS5	DMSZ	N/A
Experimental models: Organisms/strains		
Mouse: NOD.Cg-PrkdcscidIL2RGtm1wjl/SzJ (005557)	Jackson Laboratory	N/A
Oligonucleotides		
Nextera™ DNA CD Indexes	illumina	20018708
Software and algorithms		
FlowJo software (10.7)	TreeStar Inc.	N/A
Prism 9	Prism-Graphpad	www.graphpad.com
Spectro-Flo software	Cytec	
ClonAn software		http://arxiv.org/abs/1802.03426
ENCODE ATAC-seq pipeline version 1.7.2		https://github.com/ENCODE-DCC/atac-seq-pipeline

RESOURCE AVAILABILITY

Lead contact

Further information and requests for resources should be directed to and will be fulfilled by the lead contact, Bruno Canque (bruno.canque@ephe.psl.eu).

Materials availability

This study did not generate new unique reagents.

Data and code availability

- RNA-seq data have been deposited at GEO and are publicly available. Accession numbers are listed in the key resources table.
- This paper does not report original code.
- Any additional information required to reanalyze the data reported in this paper is available from the lead contact upon request.

EXPERIMENTAL MODEL AND SUBJECT DETAILS

Human sample collection

Human fetal (gestational ages 13 to 23 weeks, n = 14) or postnatal (2–87 years, n = 50) tissues from male or female donors were collected after informed consent according to institutional guidelines and the French bioethical legislation. No limitations were placed on analyzed samples in terms of donor ancestry, race, or ethnicity. Umbilical cord blood (UCB) was provided by the Unité de Thérapie Cellulaire of Hôpital Saint-Louis (Paris). Postnatal bone marrow (BM) samples were from healthy graft donors (Unité de Thérapie Cellulaire, Hôpital Saint-Louis, Paris). Fetal BMs were from spontaneously terminated pregnancies (Service de Biologie du Développement, Hôpital Robert Debré, Paris). Fetal (gestational ages 19 to 38 weeks, n = 13) and neonatal (0–77 days, n = 34) blood samples were from healthy donors (Service de Biologie du Développement, Hôpital Robert Debré, Paris).

Mice

NOD.Cg-Prkdc^{scid}IL2RG^{tm1wjl}/SzJ (005557) mice known as NOD scid gamma (NSG) mice (Jackson Laboratory, Bar Harbor, MI) were housed in the pathogen-free animal facility of Institut de Recherche Saint Louis (Paris). Female NSG mice) were xenografted at 2 months of age. The Ethical Committee at Paris Nord University approved all performed experiments.

METHOD DETAILS

Processing of human tissues and cell separation

Femurs from fetal or adult donors were sterilely excised and processed in RPMI 1640 medium supplemented with 10 U/ml RNase-free DNase I, before single-cell suspensions were filtered through a cell strainer (70 μm; BD biosciences). Blood or BM mononuclear cells were separated by Ficoll-Hypaque centrifugation (Pancoll, PAN Biotech GmbH) before processing for flow cytometry, cell sorting or CD34$^+$ HSPC isolation. CD34$^+$ HSPCs were isolated with the CD34 Microbead kit (Miltenyi Biotech; purity >90%), frozen in heat-inactivated fetal calf serum (FCS) supplemented with 10% DMSO and stored in liquid nitrogen until use.

Xeno-transplantations

NSG mice (Jackson Laboratory, Bar Harbor, MI) were housed in the pathogen-free animal facility of Institut de Recherche Saint Louis (Paris). The Ethical Committee at Paris Nord University approved all performed experiments. 3 months old mice were irradiated with 2.25 Gy 24 h before injection of 2.5 x 10^5 CD34$^+$ HSPCs in the caudal vein and sacrificed 8 weeks later. Single-cell suspensions recovered from femurs and tibias were filtered through a cell strainer (70 μm; BD biosciences) and depleted in mouse cells using the Mouse Cell Depletion Kit (Miltenyi) before being processed for Flow Cytometry.

Flow cytometry and cell sorting

Human single-cell suspensions were incubated with human Fc receptor-binding inhibitor (Fc Block, eBioscience) before surface staining with anti-human monoclonal antibodies (mAbs). Fluorescence minus one (FMO) isotype controls were used to define positive signals for flow cytometry or cell sorting. Dead cells were excluded with the Zombie Violet Fixable Viability Kit (Biolegend). For labeling, cells were resuspended in PBS, 2% FCS (1–5 x10^7 cells/500 μL) and incubated with the following mAbs: CD45 AF700 (Biolegend, clone HI30), CD34 PB (Biolegend, clone 581), CD7 FITC (Beckman Coulter, clone 8H8.1), CD38 PerCPCy5.5 (Biolegend, clone HIT2), CD33 BV785 (Biolegend, clone WM53), CD115 APC (Biolegend, clone 9-4D2-1E4), CD71 PE (BD Bioscience, clone M-A712), ITGB7 PC7 (eBioscience, clone FIB504), CD3 PE-CF594 (BD Bioscience, clone UCHT1), CD14 PE-CF594 (BD Bioscience, clone MOP9), CD19 PE-DAZZLE (Biolegend, clone HIB19), CD24 PE-CF594 (BD Bioscience, clone ML5), CD56 PE-CF594 (BD Bioscience, clone B159), CD45RA BV711 (Biolegend, clone HI100), CD116 APC-vio770 (Miltenyi, clone REA211), CD127 PC5 (Biolegend, clone A019D5), CD117 BV605 (Biolegend, clone 104D2), CD10 BV650 (BD bioscience, clone HI10a), CD123 PE-Cy5.5 (Beckman Coulter, clone SSDCLY107D2), also CD45RA PE (BD Bioscience, clone HIT100), CD19 BV711 (BD bioscience, clone HIB19). Flow cytometry and cell sorting were performed with a BD Fortessa Analyzer or a BD FACSAria III sorter (BD Biosciences; (purity $\geq$95%). Flow cytometry analyses were performed using the FlowJo software (Version 10.7).

Spectral cytometry

Human single-cell suspensions isolated from the spleen or BM of xenografted mice were processed and labeled as above were the following antibodies: CD45 PerCp (Biolegend, clone HI30), CD34 BUV615 (BD bioscience, clone 581), CD45RA BUV395 (Biolegend, clone HI100), CD38 APC-Fire 810 (Biolegend, clone HIT2), CD33 PE Texas Red (Biolegend, clone WM53), CD117 BV605 (Biolegend, clone 104D2), CD71 PECy5 (BD bioscience, clone M-A712), CD115 APC (Biolegend, clone 9-4D2-1E4), CD116 AP-Vio770 (Miltenyi, clone REA211), CD123 SB436 (BD bioscience, clone 7G3), CD127 APC R700 (Biolegend, clone A019D5), ITGB7 PECy7 (eBioscience, clone FIB504), CD7 FITC (Beckman Coulter, clone 8H8.1), CD10 BV650 (BD bioscience, clone HI10a), CD2 PerCpCy55 (Biolegend, clone RPA-2.10), CD19 Spark NIR 685 (Biolegend, clone HIB19), CD24 PE-AF 610 (Invitrogen, clone SN3), CD20 Pacific Orange (Invitrogen, clone HI47), IgM BV570 (Biolegend, clone MHM-88), IgD BV480 (Biolegend, clone IA6-2), CD5 BV785 (BD bioscience, clone UCHT2), CD56 BUV737 (BD bioscience, clone B159), CD94 PE (BD bioscience, clone HP-3D9), CD3 BUV661 (BD bioscience, clone HIT3a), CD1c AF647 (BD bioscience, clone F10/21A3), CD141 BB515 (BD bioscience, clone 1A4), CD303 BV750 (BD bioscience, clone V24-785), CD304 BV711 (Biolegend, clone 12C2), CD14 Spark Blue 550 (Biolegend, clone 63D3), CD16 BUV496 (BD bioscience, clone 3G8), CD15 BUV805 (BD bioscience, clone W6D3) and Zombie UV for dead cells. Spectral cytometry was performed with a Cytec Aurora cytometer (Spectro-Flo software). Flow cytometry analyses were performed using the FlowJo software (Version 10.7).

Cell cultures and analysis

Differentiation assays

For T cell differentiation assays, OP9-DL4 cells (1.5 x 10^3 cells/well in 200 μL; gift of A. Cumano, Institut Pasteur, Paris) were seeded in Opti-MEM-Glutamax supplemented with 10% FCS, 1% penicillin-streptomycin and 1/1000 β-mercapto-ethanol (Life Technologies) in 96-well flat-bottom plates 24 h prior to co-culture. Before cell sorting, medium was removed and 200 μL of complete medium supplemented with SCF (10 ng/mL), FLT3L (5 ng/mL), and IL-7 (2 ng/mL) (all from Miltenyi Biotech)

was added. 50 Cells were sorted directly into the wells and allowed to differentiate for 2 weeks. On culture day 7, 50 μL of complete medium supplemented with 4X cytokine concentrations were added to each well. At culture day 14, the well content was harvested, and cells were labeled with CD45 AF700 (Biolegend, clone HI30), CD34 PB (Biolegend, clone 581), CD7 BV510 (BD Bioscience, clone M-T701), CD5 APC (BD Bioscience, clone UCHT2), CD4 FITC (Biolegend, clone RPA-T4), and CD8a PC7 (Biolegend, clone RPA-T8) mAbs.

For NK differentiation assays, OP9 cells were seeded as above in 96-well flat-bottom plates 24 h prior to culture initiation. Before cell sorting, medium was removed and 200 μL of complete medium supplemented with SCF (10 ng/mL), FLT3L (10 ng/mL), IL-7 (10 ng/mL) and IL-15 (10 ng/mL) (all from Miltenyi Biotech) was added. Cells were sorted directly into the wells (50 cell/well) and allowed to differentiate for 2 weeks. On culture days 7, 50 μL of fresh medium supplemented with 4X cytokine concentrations were added to each well. At culture day 14, the well content was harvested, and cell surface staining was performed with the following mAbs: CD45 AF700 (Biolegend, clone HI30), CD7 FITC (Beckman Coulter, clone 8H8.1), CD56 PC7 (Biolegend, clone MEM-188), CD14 PE-CF594 (BD Bioscience, clone MOP9), CD94 APC (Biolegend, clone DX22). NK cells were defined as the $CD45^{+}CD14^{-}CD56^{+}$ subset.

For B cell differentiation assays, MS5 cells (1.5×10^4 cells/well) were seeded 24 h prior to co-culture initiation in 96-well flat-bottom plates with RPMI medium supplemented with 10% FCS, 1% glutamine, and 1% penicillin-streptomycin and 1/1000 β-mercaptoethanol (Life Technologies). Before cell sorting, medium was removed and 200 mL of complete medium supplemented with SCF (10 ng/mL), TPO (10 ng/mL), and IL-7 (10 ng/mL). Cells were sorted directly into the wells by pools of 50–100 cells and allowed to differentiate for 2 weeks. On culture day 7, 50 mL of complete medium supplemented with 4X growth factor concentrations were added to each well. The following antibodies were used to assess BL differentiation: CD45 AF700 (Biolegend, clone HI30), CD19 APC (Biolegend, clone HIB19), CD9 PE-CF594 (BD biosciences clone M-L13), CD7 FITC (Beckman Coulter, clone 8H8.1), CD10 BV650 (BD bioscience, clone HI10a), CD20 APC (Biolegend, clone 2H7), CD24 BV785 (BD biosciences clone ML5), CD127 PC5 (Biolegend, clone A019D5), IgM BV421 (Biolegend, clone MHM-88), IgD PC7 (Biolegend, clone IA6-2). Flow cytometry was performed as above with a BD Fortessa Analyzer and the FlowJo software.

Diversification assays

For diversification assays under bulk (100 cell/well) or clonal conditions, OP9 stromal cells were seeded as above in Opti-MEM-Glutamax supplemented with 2.5% FCS, 7.5% BIT 9500 (StemCell Technologies), 1% penicillin-streptomycin and 1/1000 β-mercapto-ethanol (Life Technologies) in 96-well U-bottom plates 24 h prior to co-culture with SCF (*scf*) or with combinations of growth/differentiation factors (10 ng/mL each; all from Miltenyi Biotec) optimized for lymphoid (*scf:tpo:tslp*), multilineage (*scf:flt3l* or *scf:gm:tpo*) or myeloid (*scf:g:gm*) differentiation (Alhaj Hussen et al., bioRxiv 2022.12.12.520022).

UCB or BM $CD34^{+}$ HSPC subsets were directly seeded by FACS in the corresponding plates and cultured for 10 (bulk cultures) or 14 (clonal cultures) days before being subjected to FACS analysis. Flow cytometry analyses were performed with a BD Fortessa Analyzer using the following antibodies: CD45 AF700 (Biolegend, clone HI30), CD34 PB (Biolegend, clone 581), CD7 FITC (Beckman Coulter, clone 8H8.1), CD123 BV786 (BD Bioscience, clone 7G3), CD115 APC (Biolegend, clone 9-4D2-1E4), CD45RA PE (BD Bioscience, clone HIT100), ITGB7 PC7 (eBioscience, clone FIB504), CD24 PE-CF594 (BD Bioscience, clone ML5), CD19 BV711 (BD bioscience, clone HIB19), CD116 APC-vio770 (Miltenyi, clone REA211), CD127 PC5 (Biolegend, clone A019D5), CD15 BV605 (BD bioscience, clone HI10a), CD10 BV650 (BD bioscience, clone HI98). Flow cytometry analyses were performed using the FlowJo software. Please note that the molecular identity and differentiation potential of in vitro-differentiated $CD127^{-/+}$ ELPs has been previously controlled (Alhaj Hussen et al., bioRxiv 2022.12.12.520022).

Chromatin accessibility mapping by ATAC-seq

Transposing reactions for ATAC-seq were performed as previously described,[48] using between 15 and 30 000 cells from the indicated populations (minimum 2 biological replicates per population). Sequencing libraries were generated using 5 cycles of PCR pre-amplification with Nextera barcoding primers[48] followed by 3–5 additional cycles, according to the quantity of pre-amplified product as detected in a qPCR side reaction.[49] Amplified libraries were size selected and sequenced (100 bases paired end) on a HiSeq 4000 to a minimum depth of 30 million raw paired reads, at the GenomeEast Platform of the IGBMC, Strasbourg, France.

Gene expression profiling by mini-RNA-seq

The protocol used for mini-RNAseq was adapted from Soumillon et al.[50] For each population batches of 100 cells (2–10 replicates) were sorted by FACS in 96-well V-bottom plate wells containing 2 μL of lysis buffer (Ultra-pure Water containing 10% Triton X-100 and RNasin plus 40U/ul). After evaporation of the lysis buffer at 95°C for 3 min, first strand cDNA synthesis was performed using Maxima H Minus Reverse Transcriptase (Thermo Fisher), E3V6NEXT primers (specific primer for each well) and Template Switching Primer: E5V6NEXT. Resulting cDNAs were then pooled and purified by DNA Clean and Concentrator TM-5 (Zymo research) and treated with Exonuclease I (New EnglandBiolabs) before amplification by the Advantage 2 PCR kit (Clontech) and the SINGV6 primer (95°C for 1 min, 15 cycles at 95°C for 15s, 65°C for 30s, 68°C for 6 min, and 72°C for 10 min). PCR products were purified by Agencourt AMPure XP (Beckman Coulter). Libraries were prepared using Illumina DNA Prep (Illumina) according to the manufacturer's guidelines and sequenced on a HiSeq 4000 at the GenomeEast Platform of the IGBMC (Strasbourg, France). Image analysis and base calling were performed using RTA 2.7.7 and bcl2fastq 2.17.1.14. Adapter dimer reads were removed using DimerRemover (https://sourceforge.net/projects/dimerremover/).

QUANTIFICATION AND STATISTICAL ANALYSIS

Algorithm-assisted clone classification

Immunophenotypic data were extracted using the FlowJo software following the gating strategy described in Figure S3A. Algorithm-assisted clone classification was based on size (absolute cell number/clone) and relative percentages of HSPCs ($CD34^+$), granulocytes ($CD15^+$), monocytes ($CD115^+$), dendritic cells ($CD123^+$) and lymphoid cells. Percentages of lymphoid cells per clone were defined as the sum of the percentages of $CD19^+$ B cells, $CD127^-$ ELPs and $CD127^+$ ELPs. Data were processed with the ClonAn software (see below) using the UMAP package (http://arxiv.org/abs/1802.03426).[51] The ClonAn software used for algorithm-assisted clone classification analyses was developed by Samuel Diop on top of the Scikit-Learn Library.[52]

ATAC-seq analysis and bioinformatics

Demultiplexed sequencing data were processed using the ENCODE ATAC-seq pipeline version 1.7.2 (https://github.com/ENCODE-DCC/atac-seq-pipeline) using the hg38 assembly and the default parameters for paired end sequencing. Only samples with TSS enrichment >5 were used in subsequent analyses. Downstream analyses were performed using the optimal peakset output (FDR<0.05) from Irreproducible Discovery Rate analysis. Peaks within 500 bp were merged using bedtools MergeBED (-d 500).[53] Reads in peaks were counted using Featurecounts[54] with default parameters for paired end reads. PCA of signal within peaks and detection of differential peaks (log_2 fold change>0.5; padj<0.05) were carried out using EdgeR with TMM normalisation and robust conditions.[55] Coverage bigwig files were generated with bamCoverage (deepTools2)[56] using TMM-normalisation factors and were visualised on the UCSC genome browser together with Encode ChIP-seq tracks of H3K4me1 and H3K27ac in K562 and GM12878 ("https://www.encodeproject.org"). Normalised bigwig files were used to generate heatmap and pileup profiles using computeMatrix (scaled region mode; 1 kb flanking each peak, sorting on mean peak signal) followed by plotHeatmap (deepTools2). Distribution of peaks relative to genomic features (hg38) was analyzed with ChIPseeker at default settings except with promoters defined as +- 500 bp of the TSS.[57] Ontology analysis of genes associated with ATAC peaks was performed with the GREAT tool (v4.0.4) (3http://great.stanford.edu/public/html/"),[58] using the whole hg38 genome as background and applying association settings of Basal plus extension, proximal windows of 2 kb upstream and 1 kb downstream, plus distal up to 1 Mb and including curated regulatory domains. Motif analysis was performed using the XSTREME tool (v5.4.1) (Charles E. Grant and Timothy L. Bailey, "XSTREME: comprehensive motif analysis of biological sequence datasets", *BioRxiv*, 2021). of the MEME suite[59] at default parameters, using background sets of unchanging peaks of equivalent sizes to the test peaksets.

Mini-RNA-seq analysis and bioinformatics

Data quality control and preprocessing

Data quality control and pre-processing were performed by SciLicium (Rennes, France). Briefly The first read contains 16 bases that must have a quality score higher than 10. The first 6 bp correspond to a unique sample-specific barcode and the following 10 bp to a unique molecular identifier (UMI). The second reads were aligned to the human reference transcriptome from the UCSC website using BWA version 0.7.4.4 with the parameter "–l 24". Reads mapping to several positions in the genome were filtered out from the analysis. The complete pipeline has been previously described in.[60] After quality control and data pre-processing, a gene count matrix was generated by counting the number of unique UMIs associated with each gene (lines) for each sample (columns). The UMI matrix was further normalized with the regularized log (rlog) transformation package implemented in the DeSeq2 package.[61] Raw and pre-processed data are accessible on Gene Expression Omnibus (GEO): GSE215045; GSE215052.

Statistical filtration and clustering analysis

The statistical comparisons were performed in the AMEN suite of tools.[62] For each transcriptomic analysis, several relevant comparisons were selected to identify differentially expressed genes (DEGs). Briefly, genes showing an expression signal higher than 0.0 and at least a 2.0-fold-change between the two experimental conditions of each pairwise comparison were selected. The empirical Bayes moderated t-statistics implemented into the LIMMA package (F-value adjusted using the Benjamini & Hochberg (BH) False Discovery Rate approach, $p \leq 0.05$)[63,64] was used to define the set of genes showing significant statistical changes across all comparisons of a given transcriptomic analysis. The resulting set of DEGs were then clustered into distinct expression clusters with the k-means algorithm and presented as heatmaps by using the pheatmap R package developed by R. Kolde (2019) (version 1.0.12. "https://CRAN.R-project.org/package=pheatmap").

Functional analysis and regulatory network analysis

Gene Ontology enrichment analysis was performed with the AMEN suite.[62] A specific annotation term was considered enriched in a gene cluster when the FDR-adjusted p value was ≤ 0.05 (Fisher's exact probability). The regulatory network representations were drawn using the igraph package ("https://igraph.org") (Csardi & Nepusz, 2006) implemented in R. The regulation data described correspond to a consolidation of all gene sets provided by GSEA[65] associated with transcription factor targets. Those transcription factor target prediction gene sets are based on the Gene Transcription Regulation Database (GTRD)[66] and legacy sets, the latter corresponding to upstream cis-regulatory motifs.[67]